

Equator and High-Latitude Ionosphere-to-Magnetosphere Research

**B. W. Reinisch
G. S. Sales
V. Paznukhov
I. A. Galkin
D. F. Altadill
G. Khmyrov**

**Center for Atmospheric Research
University of Massachusetts Lowell
600 Suffolk Street
Lowell, MA 01854**

Scientific Report No. 1

30 October 2007

APPROVED FOR PUBLIC RELEASE; DISTRIBUTION UNLIMITED.



**AIR FORCE RESEARCH LABORATORY
Space Vehicles Directorate
29 Randolph Road
AIR FORCE MATERIEL COMMAND
Hanscom AFB, MA 01731-3010**

20080624 204

NOTICE AND SIGNATURE PAGE

Using Government drawings, specifications, or other data included in this document for any purpose other than Government procurement does not in any way obligate the U.S. Government. The fact that the Government formulated or supplied the drawings, specifications, or other data does not license the holder or any other person or corporation; or convey any rights or permission to manufacture, use, or sell any patented invention that may relate to them.

This report was cleared for public release and is available to the general public, including foreign nationals. Qualified requestors may obtain additional copies from the Defense Technical Information Center (DTIC) (<http://www.dtic.mil>). All others should apply to the National Technical Information Service.

AFRL-RV-HA-TR-2007-1152 HAS BEEN REVIEWED AND IS APPROVED FOR
PUBLICATION IN ACCORDANCE WITH ASSIGNED DISTRIBUTION STATEMENT.

//Signature//

KENNETH R. WALKER
Contract Manager

//Signature//

JOEL MOZER, Chief
Space Weather Center of Excellence

This report is published in the interest of scientific and technical information exchange, and its publication does not constitute the Government's approval or disapproval of its ideas or findings.

REPORT DOCUMENTATION PAGE

Form Approved
OMB No. 0704-0188

1. The reporting burden for this collection of information is estimated to average 1 hour per response, including the time for reviewing instructions, searching existing data sources, gathering and maintaining the data needed, and completing and reviewing this collection of information. Send comments regarding this burden estimate or any other aspect of this collection of information, including suggestions for reducing the burden to Department of Defense, Washington Headquarters Services, Directorate for Information Operations and Reports (0704-0188), 1215 Jefferson Davis Highway, Suite 1204, Arlington, VA 22202-4302. 2. Respondents should be aware that notwithstanding any other provision of law, no person shall be subject to any penalty for failing to comply with a collection of information if it does not display a current OMB control number. PLEASE DO NOT RETURN YOUR FORM TO THE ABOVE ADDRESS.

REPORT DATE (DD-MM-YYYY)

01-10-2007

2. REPORT TYPE

Scientific Report No. 1

3. DATES COVERED (From - To)

25 Aug 2006 - 25 Aug 2007

TITLE AND SUBTITLE

Equator and High-Latitude Ionosphere-to-Magnetosphere Research

5a. CONTRACT NUMBER

FA8718-06-C-0072

5b. GRANT NUMBER

5c. PROGRAM ELEMENT NUMBER

62601F

AUTHOR(S)

W. Reinisch, G.S. Sales, V. Paznukhov, I.A. Galkin, D.F. Altadill, G. Khmyrov

5d. PROJECT NUMBER

4827

5e. TASK NUMBER

HR

5f. WORK UNIT NUMBER

A1

PERFORMING ORGANIZATION NAME(S) AND ADDRESS(ES)

Center for Atmospheric Research
University of Massachusetts Lowell
100 Suffolk Street
Lowell, MA 01854

8. PERFORMING ORGANIZATION REPORT NUMBER

SPONSORING / MONITORING AGENCY NAME(S) AND ADDRESS(ES)

Air Force Research Laboratory
1 Randolph Road
Wright-Patterson AFB, MA 01731-3010

10. SPONSOR/MONITOR'S ACRONYM(S)

AFRL/RVBXI

11. SPONSOR/MONITOR'S REPORT NUMBER(S)

AFRL-RV-HA-TR-2007-1152

DISTRIBUTION / AVAILABILITY STATEMENT

Approved for public release; distribution unlimited.

SUPPLEMENTARY NOTES

ABSTRACT

This report describes significant improvements in digital sounder technology as applied to ionospheric research in the equatorial, mid and high-latitude regions. These new developments are in the areas of ionospheric drift, radio-wave absorption, precision group-height and the specification of sounder measurement uncertainty. Ultimately these techniques are to be included into routine sounder operations and ARTIST performance. These developments required research, which is reported here, into the structure of the ionospheric layers, including the D-region, and the E and F layers. In addition, a major effort under this project involved ionospheric profile validation; that is comparing sounder measured electron density profiles with the results of other techniques. These comparisons were made using the data from other researchers including tomographic, occultation and DMSP UV measurements. Finally, the effects of strong magnetic storms on a dense network of sounders in Europe are presented. Large changes in the ionosphere were observed in the daytime on disturbed days and the latitudinal response of ionosphere was analyzed and compared to similar observations at American longitudes where a very different response was observed.

SUBJECT TERMS

Magnetic storms, Ionospheric drift, Radio absorption, Profile validation, ARTIST performance

SECURITY CLASSIFICATION OF:

REPORT
U

b. ABSTRACT
U

c. THIS PAGE
U

17. LIMITATION
OF ABSTRACT

SAR

18. NUMBER
OF PAGES

76

19a. NAME OF RESPONSIBLE PERSON
Kenneth R. Walker

19b. TELEPHONE NUMBER (include area code)

Contents

1. INTRODUCTION	1
2. COMPARISON OF THE IONOSPHERIC PROFILES DERIVED USING A RADIO OCCULTATION TECHNIQUE TO THE DIGISONDE DATA 1	1
2.1 Introduction	1
2.2 Data Collection	2
2.3 Data Analysis	3
2.4 Conclusions and Future Efforts	9
3. ARTIST UNCERTAINTY SPECIFICATION	10
3.1 Introduction	10
3.2 Approach	10
3.3 Statistical Analysis of ARTIST Performance Against Manual Data	11
3.3.1 General Approach	11
3.3.3 ARTIST Confidence Level of Autoscaling and Uncertainty	12
3.3.4 Calculating Uncertainty Bounds	13
3.3.5 Boulder Digisonde Dataset	14
3.3.6 Classification by Spread F Severity Level and CLA	15
3.3.7 Uncertainty Associated with Different Versions of ARTIST	17
3.3.8 Station-Specific Uncertainty	18
3.4 Reporting Uncertainties in SAO Format	19
3.4.1 Uncertainty Bounds for N(h) Profiles	19
3.4.2 Software Modifications	19
3.5 Future Efforts	20
4. DIGISONDE GROUND-TRUTH DATA FOR THE NWRA TOMOGRAPHY VALIDATION PROJECT	21
5. PRECISION GROUP HEIGHT MEASUREMENTS OF E LAYER VIRTUAL HEIGHTS	21
5.1 Introduction	21
5.2 The Virtual Height Phase Technique	22
5.3 Measuring E Layer Heights at Millstone Hill	25
6. PROCESSING OF DIGISONDE DRIFT MEASUREMENTS	29
6.1 Introduction	29
6.2 Data Analysis	30
6.3 Future Efforts on Drift Data Analysis	34
6.4 DDA Software Upgrade	35
7. STUDY OF THE IONOSPHERIC RESPONSE TO STRONG GEOMAGNETIC STORMS	35
7.1 Introduction	35
7.2 Data Analysis	36

7.2 Data analysis	36
7.3 Discussion	42
7.4 Summary	44
8. ROUTINE HF ABSORPTION MEASUREMENTS USING DIGISONDES	45
8.1 Approach	45
8.2 System calibration	46
9. FOCUSING AND REFLECTION CALCULATIONS	48
9.1 Focusing gain	48
9.2 Nighttime F-layer reflectivity	52
9.3 Reflectivity theory	54
10. CALIBRATION / VALIDATION OF DMSP UV MEASUREMENTS OF THE F2 PEAK CHARACTERISTICS WITH DIGISONDE MEASUREMENTS	57
11. PUBLICATIONS	61
REFERENCES	63

Figures

1. A COSMIC satellite pass over the Athens digisonde on December 21, 2006. The blue symbols show radial projections of the ray path tangent points. The red star indicates the station location. 3
2. Athens ionograms recorded during the occultation on December 21, 2006 at 0800 UT and 0815 UT. 4
3. Comparison of the digisonde and COSMIC RO profiles for Athens. The plots show the electron density (top figure) and plasma frequency (bottom) as a function of height. 5
4. Comparison of the Ascension Island profiles derived from digisonde and COSMIC RO measurements (plots on the left) obtained on December 20, 2006. On the right is the measured ionogram demonstrating spread F conditions. 6
5. Comparison of the Kwajalein Island profiles obtained from digisonde and COSMIC RO measurements on December 21, 2006. 7
6. RO tangent points (blue) near Zhigansk and Yakutsk digisonde stations on December 21, 2006 8
7. RO measurements on December 21, 2006 in the vicinity of Zhigansk and Yakutsk digisonde stations. 8
8. Comparison of foF2 values deduced from simultaneous digisonde and RO measurements. 9
9. Point-by-point uncertainty of the ARTIST electron density profile is obtained by Calculating inner and outer boundaries enclosing the profile. Both boundaries rest on five anchor points whose uncertainties are known from statistical analysis of manually evaluated differences between automatically and manually scaled values. 10
10. A digisonde ionogram recorded during severe spread F conditions in Jicamarca, Peru (left). 12
If multiple echoes are resolved and presented as individual edgels (right), the trace extraction algorithm is overwhelmed with numerous possibilities of grouping edgels to traces.
11. Cumulative difference function of the absolute |autoscaled-manual| differences for a rapid 13
evaluation of ARTIST uncertainty. ARTIST-5 reports of foF2 for Grahamstown have 0.15 MHz uncertainty at 95% level.

12. Uncertainty bounds for foF2 derived from the frequency histogram of (ARTIST-manual) differences for Boulder Digisonde 256 ionograms. For 12,612 ionograms scaled with confidence (87% of total 14,501 ionograms), the uncertainty bounds at 5% percentile are -0.25 and +0.35 MHz.	14
13. Availability of manually interpreted data for the Boulder Digisonde station. The plot shows foF2 for every processed ionogram for years 2004-2006.	15
14. ARTIST 4.5 uncertainty calculated for the winter and summer time for Boulder digisonde. Plots show foF2 cumulative differences calculated for nighttime (black) and daytime (red) ionograms for each period.	16
15. Uncertainty of foF2 autoscaled value for Gakona, AL digisonde as a function of automatically detected level of spread F conditions. Comparison of ARTIST 5.0.2-b7 results for 5474 manually scaled ionograms during the 2002-2006 period.	16
16. Cumulative difference characteristics for Boulder 2004 ionograms. This figure compares the results obtained with ARTIST5.0 left) and ARTIST4.5 (right). Numerical values for foF2, foF1, and foE scaling uncertainties (calculated at 95% level) are listed as well.	17
17. Calculated profile uncertainty boundaries shown in the SAO Explorer.	20
18. Distribution of virtual heights during one sounding made on 14 September 2006 at 1422 UT. A majority of the calculated heights are concentrated within a single statistical range bin at 107.5 ± 0.5 km.	26
19. Daily E region precision group heights at Millstone Hill as function of time. The horizontal axes represent time (Universal Time), and the vertical axes represent virtual height (km). Dashed circles highlight significant decreases in E layer virtual heights and the black arrows point to hook-shaped disturbances.	27
20. Average daily variations of the h'E obtained from the 20 days of September. Vertical error bars indicate the standard deviation obtained at a given time.	28
21. Daily pattern of the vertical velocity data from the Ebro digisonde for December 2004. The 15 minute median values of Vz are shown as gray dots. The vertical error bars indicate the range of 80% of Vz values for each given time. The solid line represents the daily pattern calculated as a sum of the primary diurnal harmonics. The vertical dashed lines indicate the sunset (SS) and sunrise (SR) above the station at an altitude of 300 km.	30
22. Seasonal variations of the amplitudes (left) and phases (right) of the daily pattern of the Vz in the F region. The top plots show the diurnal component, the middle and bottom ones correspond to the semidiurnal and terdiurnal component, respectively.	31
23. The left panel shows the seasonal variation of the phase of the semidiurnal harmonic	31

(full line with full dots), the time of the minimum values of the daily pattern of V_z (dashed line with open squares) and the sunrise time at 300 km height (full line with open circles). The right panel shows the scatter plot of the semidiurnal phase against the sunrise time for a given month. Solid line is the best linear fit with the correlation coefficient indicated.

24. Monthly averaged east-west drift velocity data measured at Jicamarca station in 2006. 33
25. Amplitude spectra of the east-west plasma velocity measured at Jicamarca in 2006. 34
Bottom axis shows the frequency in μHz while the top axis shows the corresponding time periods in hours.
26. Geomagnetic storm of 24 August 2005. The top panel shows SYM-H index variations, 37
and the next panels show the solar wind plasma density, plasma speed, and the last two panels show the interplanetary magnetic field components. The solar wind and IMF data were taken using the ACE satellite and were shifted by 40 minutes to account for the position of the satellite.
27. Electron density profile variations as a function of time for the listed European stations 38
(see Table 5). The right panel shows storm day (August 24, 2005) data, while the left panel shows the quiet day average data. Electron density is presented in terms of equivalent plasma frequency (color bar). Sunrise and sunset times are indicated for the Ebro station with red and black circles correspondingly.
28. Variation of foF2 and hmF2 layer parameters on 24 August 2005 compared to the quiet 39
day averages (black curves). Top panel shows DST index.
29. American sector data for 24 August 2005 storm. Plots show variations of foF2 (left) and 40
hmF2 (right) as compared to the quiet day averages (black curves).
30. Difference between hmF2 values measured on the event day and the quiet day average as 41
a function of time after storm commencement.
31. August 24, 2005 storm. Color scale shows the energy input determined from radar and 43
DMSP satellite measurement. These data are taken from OVATION database. The locations of selected digisonde stations as well as Bjørnøya magnetic observatory are shown in the plot.
32. Variations of the ΔhmF2 (black) and ΔfoF2 (blue) parameters measured in the European 44
sector. The increase in the electron density lags height increases at all stations. A vertical line indicates the storm commencement time (SST). The sloping lines connect the starts of the increases in hmF2 (black line) and foF2 (blue line).
33. Number of amplitude measurements used to determine the average $P_T G_T G_R$ as a function 46
of sounding frequency.

34. Histogram of the digisonde derived $P_T G_T G_R$ values over the nighttime period from May through August 1005 for 2.9 MHz.	47
35. Illustration of focusing and defocusing gain associated with an irregular reflecting surface.	49
36. Distribution of 100 realizations of an irregular reflecting surface with RMS amplitudes varying from 0.1 through 5.0 km. In all cases the horizontal scale size was ≈ 6.8 km.	50
37. Percentage positive and negative focusing gain as a function of horizontal structure size for several vertical RMS amplitudes: a) 5 km, b) 10 km, c) 15 km and d) 20 km.	51
38. Boulder measured nighttime loss (05-09 UT) on five sequential days.	53
39. Mean loss over the hours from 05-09 UT on sequential nights from 3 May – 7 May 2005 (dots). Calculated mean F-layer slope (km/MHz) using the ionograms for the period from 1 May-7 May 2005 (squares).	54
40. Reflection index ($20 \log R $) as a function of sounding frequency for normalized layer thicknesses varying from 2 (thinnest) to 250 (thickest) in three factors of 5. (Rawer and Suchy, p. 194, Figure 64)	55
41. Reflection loss (dB) as a function of normalized layer thickness for two collision frequencies.	56

Tables

1. <i>M</i> -criterion values for four categories of the spread F condition	12
2. ARTIST uncertainty for various digisonde locations	18
3. Current state of digisonde data acquisition and processing for NWRA GPS Tomography project	21
4. Typical precision group height uncertainties for the characteristic regions of the ionosphere	25
5. Digisonde station coordinates	36
6. Maximum focusing gain and associated irregularity horizontal structure size as a function of RMS amplitude	52
7. CalVal Digisonde Data Request Status	58

1. INTRODUCTION

This research contributes in critical areas toward the goals of (1) ionospheric effects on DoD systems research and (2) ionospheric research technology.

Based on the proposal submitted to the Air Force, this year's efforts, as described in this report, involve support to the ionospheric specification objectives of the Air Force Research Laboratory (AFRL). The University of Massachusetts Lowell Center for Atmospheric Research (UMLCAR) has taken an approach that addresses the specification of ionospheric parameters on a global scale; a goal that is particularly facilitated using the digisonde system pioneered by UMLCAR. Global ionospheric modeling is a major part of space weather forecasting and global communications progress, and our support for these goals is presented here. Use of the ubiquitous digisonde offers the best tool for real time ionospheric assimilative modeling as well as support to other systems that require verification and validation. A significant part of our research effort was providing the necessary validation of other methods of ionospheric specification by using the digisonde measurements as the "truth" against which the performance of other systems was compared. These include cooperation with groups making ionospheric radio occultation and tomography, and UV measurements (Sections 2, 4, and 10). The Center is also evaluating the digisonde drift measurements against incoherent scatter radar plasma drift measurements (Section 6). The second major research concentration in this report involves the development of techniques that expand global ionospheric specification (Sections 3, 5, and 8). These cover the areas of digisonde profile uncertainty, improved ionogram virtual height measurements, and using digisondes to carry out routine measurements of the absorption of HF radio waves with the aim of predicting system outages with improved sensitivity.

Finally, this report presents the study of the effects of geomagnetic storms on the structure of the ionosphere over a wide range of latitudes and longitudes (Section 7), again, addressing the goals of global modeling.

2. COMPARISON OF THE IONOSPHERIC PROFILES DERIVED USING A RADIO OCCULTATION TECHNIQUE TO THE DIGISONDE DATA

2.1 Introduction

The development of global ionospheric models in the frame of the "space weather" concept presents the challenge of establishing a global observing network for monitoring the Earth's ionosphere. One promising technique suitable for establishing a foundation for such an ambitious project is the radio occultation (RO) method that allows reconstructing ionospheric density profiles over a large altitude range and has the natural advantage of making measurements on a global scale. Of course, a significant number of satellites is needed to provide adequate coverage of the global ionosphere but, with advances in space technology, this could eventually be achievable at a reasonable cost. At the present stage of development and testing of the RO method for the ionosphere sensing, it is most important to verify the accuracy of these measurements using an established ionospheric technique. Over the past year, we have worked

on the verification of the RO measurements made on the COSMIC satellites by using ground-based digisonde profile measurements at various locations. Our results are reported here.

2.2 Data Collection

The COSMIC/FORMOSAT-3 (Constellation Observing System for Meteorology, Ionosphere, and Climate, and Taiwan's Formosa Satellite Mission #3) is a joint Taiwan-U.S program. The project was launched in December of 2005, and is expected to continue providing data for five years. The COSMIC/FORMOSAT-3 program consists of the six spacecraft, each with three instruments, including a GPS RO receiver, an ionospheric photometer, and a tri-band beacon. The mission is aimed at space weather and climate research and forecasting, as well as geodesy and gravity research.

On 20-21 December 2006, a joint multi-instrument campaign was carried out in support of the COSMIC/FORMOSAT mission. One of the primary objectives of this campaign was to validate the electron density profiles determined using the radio occultation technique. Among the instruments participating in the campaign were 40 digisondes distributed around the globe. From December 19 until December 22, 2006, most of the digisonde stations in this program increased their measurement cadence to 5 minutes. All collected data were archived in the Digital Ionogram Database (<http://ulcar.uml.edu/DIDBase/>), and the World Data Centers archived the auto-scaled characteristics and profiles, making these data available to the scientific community.

Our aim was to establish under what conditions the RO technique is able to correctly derive the F2 layer profiles, especially, the peak characteristics f_oF_2 and h_mF_2 , as well as the E layer characteristics f_oE and h_mE , and what are the typical errors. In cases of good agreement of the F2 peak characteristics, the shapes of the bottom and topside profiles were compared. We started the comparison by preparing a list of times where RO profiles over or near Digisonde stations were expected. For these times, the digisonde autoscalings were manually edited and the edited data were added to the DIDBase archive. We have processed about 70% of the predicted cases for the December 20-21, 2006, campaign. Unfortunately, not all the predicted satellite occultations produced successful electron density profiles, especially at high latitude and equatorial regions. Thus, we were able to collect only 25 simultaneous measurements for which both digisonde and RO profiles existed.

To be exact, the RO density profile does not represent an actual vertical profile for the tangent point, but rather an average density profile representative for the ray path tangent points. The assumption of local spherical symmetry of the density distribution in a large region (up to a few thousand kilometers) is used in order to retrieve the vertical profiles. The size of the region for which this assumption was applied is characterized by a smear parameter, which is the horizontal distance between the top and bottom tangent points of the measurements. In the December 2006 campaign, for the observations of interest, smear factors varied from several hundred to a few thousand kilometers. The next section summarizes the results of the comparisons.

2.3 Data Analysis

The first example used the occultation measurements from 0758 UT to 0815 UT on 21 December 2006 made near the Athens DPS-4 digisonde station (38.0° N; 23.5° E). In Figure 1, the radial projections, onto the Earth's surface, of the RO tangent points are plotted in blue; the station location is indicated by the red star. For this observation, the COSMIC RO measurements were made close to the digisonde location, with a moderately large RO smear parameter of about 1010 km.

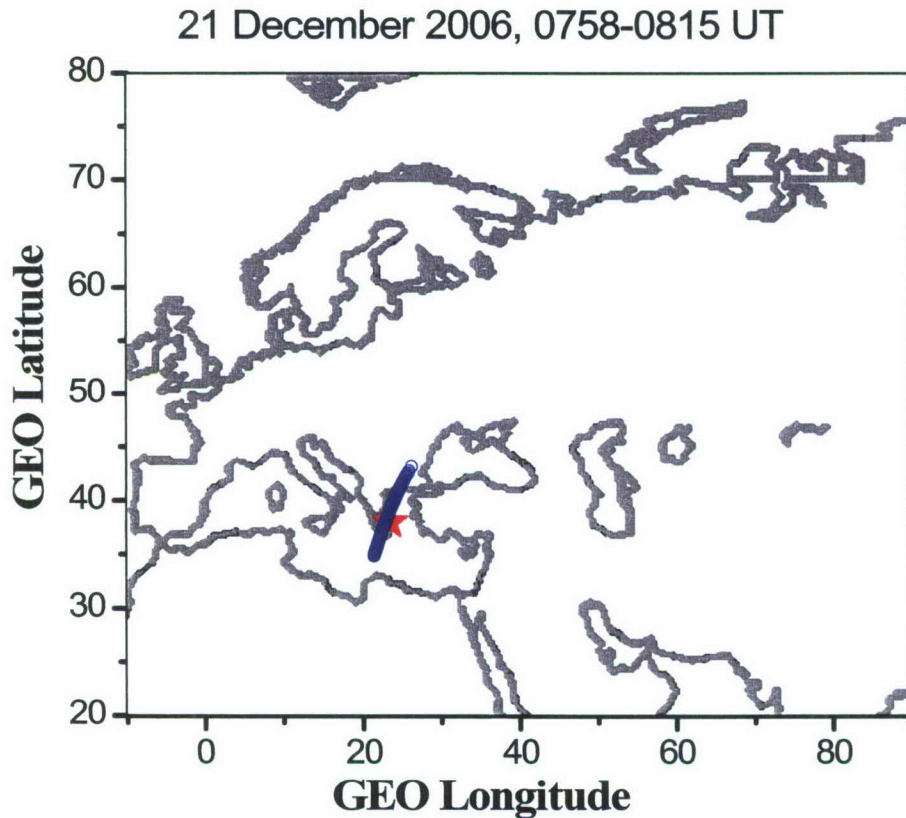


Figure 1. A COSMIC satellite pass over the Athens digisonde on December 21, 2006. The blue symbols show radial projections of the ray path tangent points. The red star indicates the station location.

Figure 2 presents the ionograms recorded at 0800 UT (10 LT) and 0815 UT. It usually takes about three minutes to complete an ionogram scan so, more precisely, the ionograms presented cover the periods 0800-0803 UT and 0815-0818 UT, respectively. These are very clean early morning ionograms with unambiguous F traces and well-defined F layer critical frequencies, foF2. No E layer trace is visible because of poor signal-to-noise conditions in the lower frequency range at the Athen's site. These plots also show the derived electron density profiles

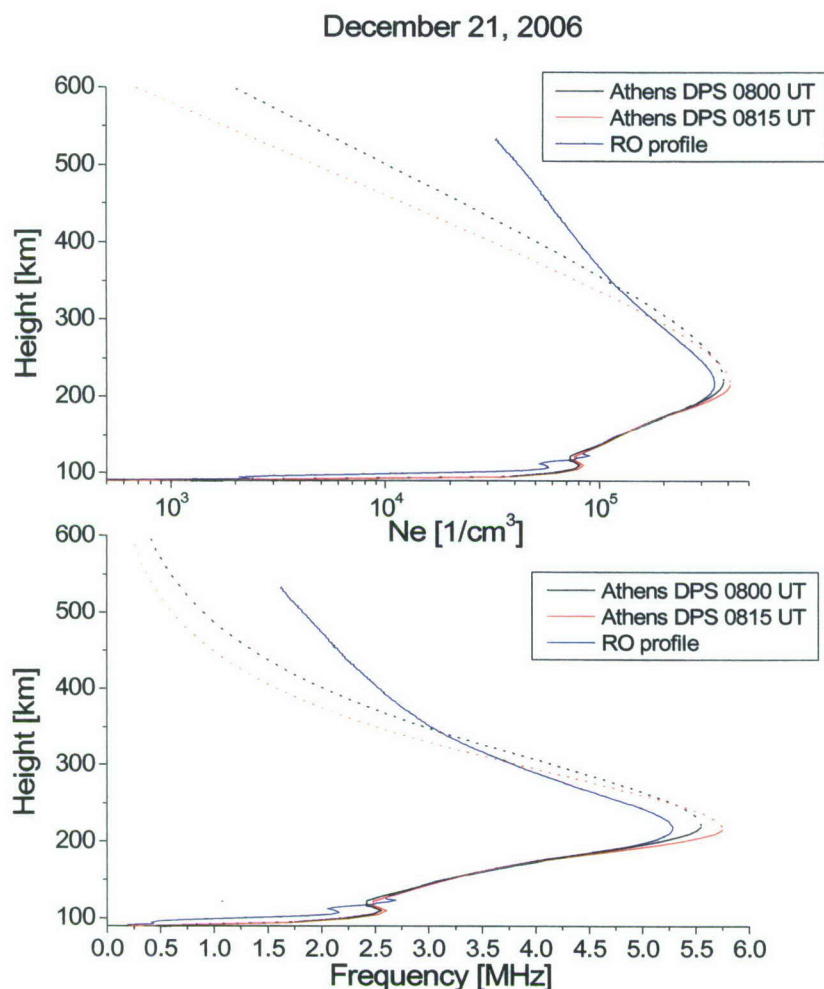


Figure 3. Comparison of the digisonde and COSMIC RO profiles for Athens. The plots show the electron density (top figure) and plasma frequency (bottom) as a function of height.

Overall, the RO profile is in reasonable agreement with the digisonde profile, although the RO peak density is somewhat smaller than the measured digisonde values. The RO measurement of foF2 was ~ 0.25 MHz smaller than the digisonde measurement made at 0800 UT and ~ 0.45 MHz smaller than digisonde foF2 measurement at 0815 UT. The lower part of the RO F2 profile is in very good agreement with the F2 digisonde profile. The digisonde E region profile is modeled (essentially using the IRI model), so no comparison should be made. Directly above the F2 peak, the RO profile is slightly thinner than the digisonde profile, and the opposite is true above 350 km. It has been shown that the topside α -Chapman profile is accurate only for the first ~ 200 km above hmF2 [Reinisch et al., 2007; McNamara et al., 2007], so comparisons above

this height are not meaningful. For this particular measurement, the RO profile shows a reasonably close agreement with the measured Ne profile over Athens.

To assess the RO performance for the low latitude ionosphere, a comparison was made with the digisonde measurements at Ascension Island (7.9° S; 345.6° E). Figure 4 shows the RO and digisonde profiles for December 20, 2006, at 2330 UT (2230 LT) on the left side, and the measured nighttime ionogram on the right. The range and frequency spread in the ionogram, typical for nighttime at this equatorial anomaly station, indicates small- and medium-scale irregularities in the F region. However, the local foF2 value was reasonably accurately measured as 8.5 ± 0.3 MHz. The RO tangent point projection passed directly over the station and the smear length was about 1000 km.

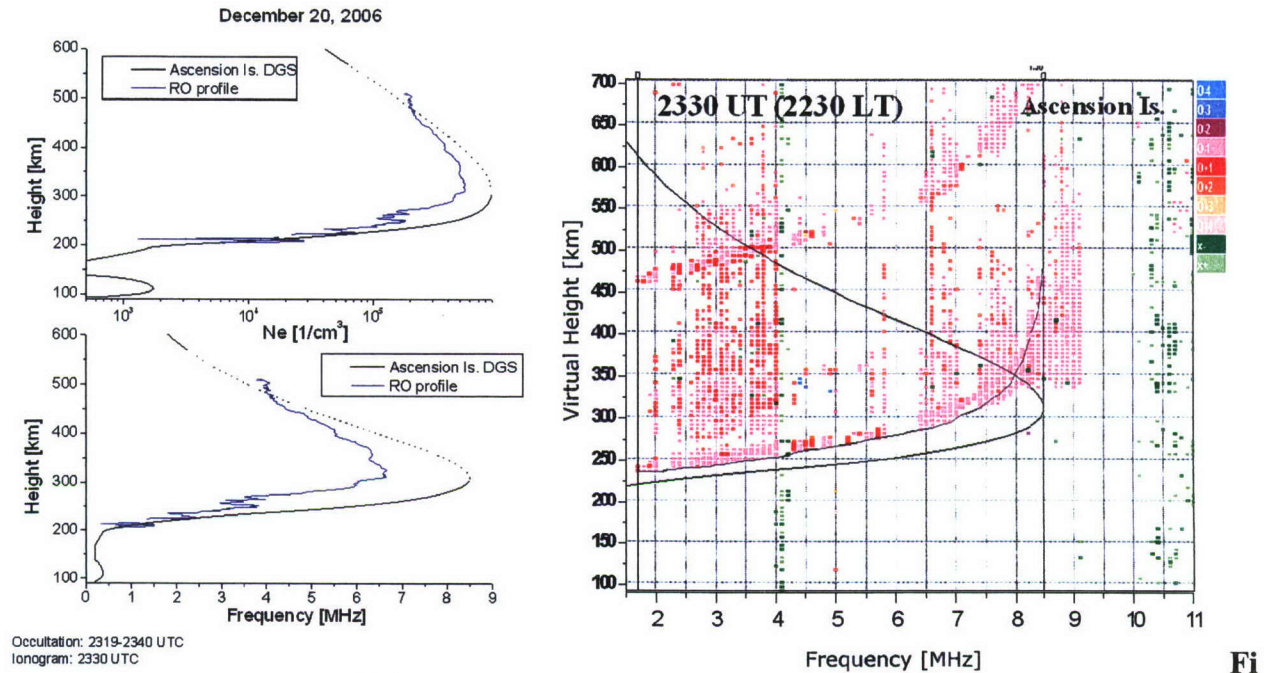


Figure 4. Comparison of the Ascension Island profiles derived from digisonde and COSMIC RO measurements (plots on the left) obtained on December 20, 2006. On the right is the measured ionogram demonstrating spread F conditions.

In this case, the RO technique significantly underestimates the peak density by ~ 2 MHz or 30% in terms of plasma frequency, or $\sim 60\%$ in terms of Ne . Clearly, in this situation, the RO profile is not an accurate description of the profile at Ascension Island.

The next example compares the RO measurements made near another equatorial digisonde station, Kwajalein Island (9.4° N; 167.4° E) on December 21, 2006, at 1220 UT (2320 LT). In this case, the RO peak density is very close to the digisonde value (only 0.25 MHz lower), but the RO bottomside profile is completely wrong. The ionogram shows a local sporadic E layer with foEs = 2.7 MHz, and probably the presence of the Es layer has affected the RO profile inversion.

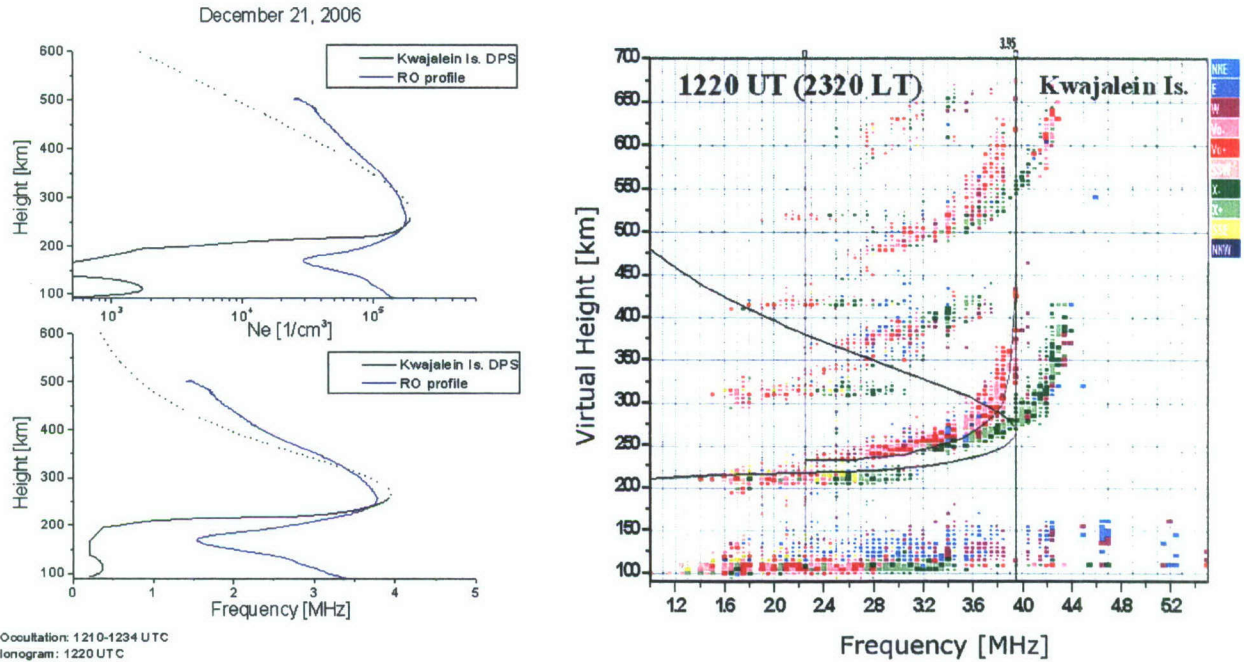


Figure 5. Comparison of the Kwajalein Island profiles obtained from digisonde and COSMIC RO measurements on December 21, 2006.

The last example is for high latitude observations near two Siberian stations: Zhigansk (66.8° N; 123.4° E) and Yakutsk (62.0° N; 129.6° E). Figure 6 shows the location of the two stations and the tangent point footprints for an RO measurement on December 21, 2006. The distance between the digisonde stations is 610 km. The occultation of December 21, 2006, was closer to the Yakutsk station (see Figure 6), and the horizontal smear of this occultation was 1417 km. Figure 6 illustrates the geometry of these measurements, and Figure 7 compares the electron density profiles at the two stations with the RO profile on December 21, 2006, at 0150 UT (0950 LT). The right panel shows the ionograms made at the two stations at this time. Clearly, the digisonde measured peak electron density is significantly lower at Zhigansk than at Yakutsk. It is possible that the Zhigansk station was located inside the mid-latitude trough at that time. The RO profile is more similar to the Yakutsk digisonde profile than the Zhigansk profile. For this particular measurement, the RO profile footprint essentially extended longitudinally (see Figure 6), and with the trough located north of Yakutsk, it probably did not seriously affect the RO inversion. However, in situations with significant latitudinal smear over ~1000 km, the mid-latitude trough would likely complicate the RO inversion. In the present example, the relatively thick E layer with $f_oE = 2.2$ MHz at ~150-km altitude, as indicated by the RO profile, was not confirmed by the Yakutsk ionogram.

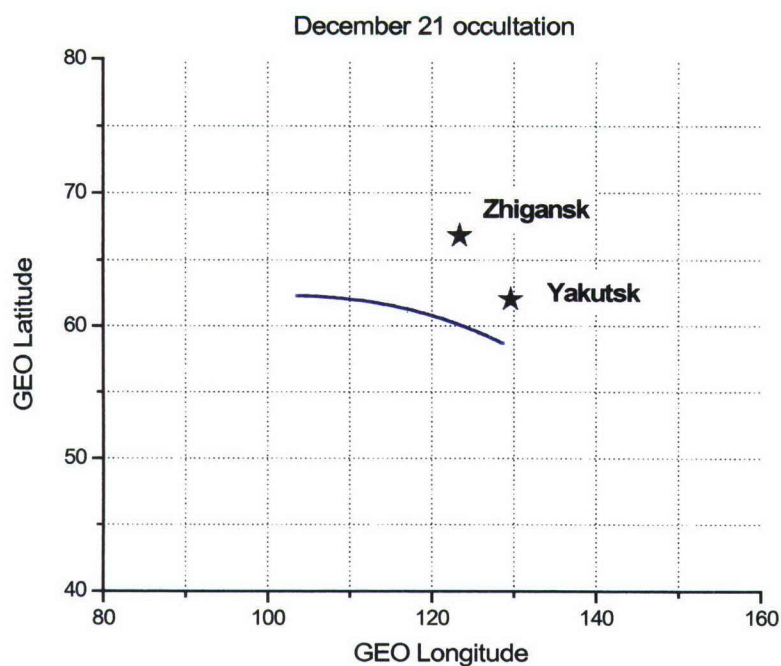


Figure 6. RO tangent points (blue) near Zhigansk and Yakutsk digisonde stations on December 21, 2006

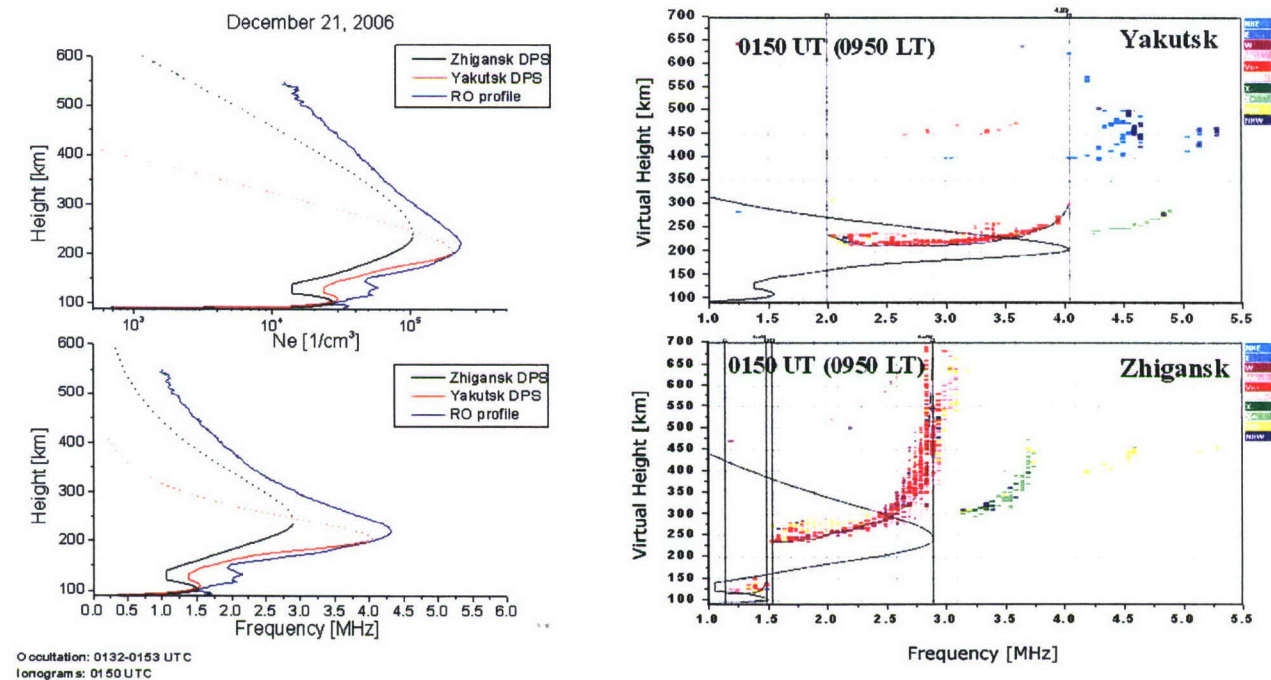


Figure 7. RO measurements on December 21, 2006, in the vicinity of Zhigansk and Yakutsk digisonde stations.

Finally, for all 25 overpass events analyzed (20 and 21 December 2006), the foF2 values determined from the digisonde ionograms and the corresponding RO measurements were compared.

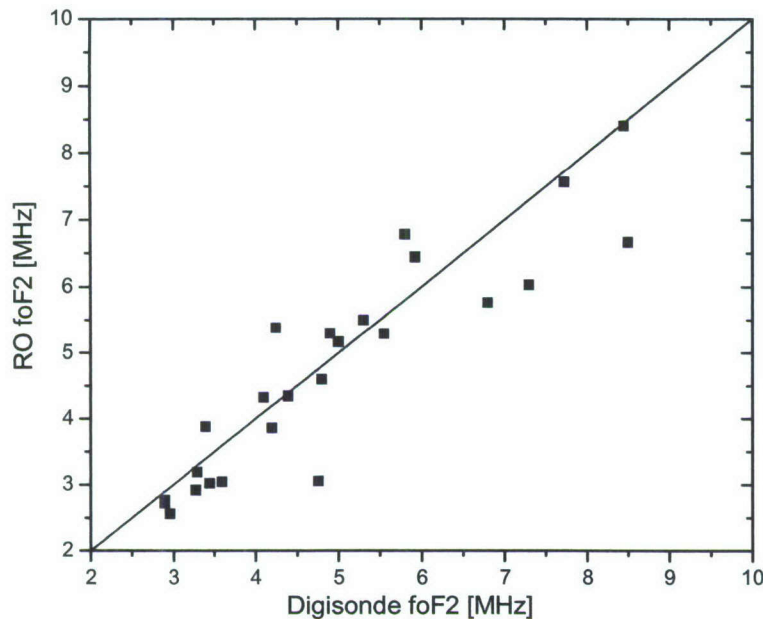


Figure 8. Comparison of foF2 values deduced from simultaneous digisonde and RO measurements.

Statistically, the RO-measured foF2 values lie reasonably close to those obtained from the digisonde observations. Out of 25 cases, there are five foF2 measurements with an error over 1 MHz; all other measurements are within this error margin. Larger errors appear to be associated with larger foF2 values.

2.4 Conclusions and Future Efforts

The results of these comparisons are interesting, and we now plan to continue analyzing data for other time periods and locations. For the amount of data analyzed, the RO measurements of the foF2 values on average were close to those measured by colocated digisondes with a typical difference of less than 1 MHz. There were, however, a few cases in which significantly larger differences were observed. These more extreme measurements appear to be associated with the equatorial region. It also should be pointed out that for the December 21-22, 2006, campaign, we were unable to make a data comparison for the high-latitude region because the predicted occultations over the digisonde stations in this region did not produce ionospheric profiles. In our future work, we will select several of the most representative digisonde sites for which more comprehensive comparison will be made. In the last quarter, we had developed a software code for extracting and processing files in the raw CDF (common data format) that are stored in the COSMIC database. This will significantly speed up data analysis since we will not have to manually select the files from the database relying on calculated satellite positions as in the past.

With this tool, it will be possible to accumulate enough data for the comparison in equatorial, middle, and high latitude regions. Our ultimate objective is to construct a statistical picture of the validity of the RO technique and to establish its advantages and limitations.

3. ARTIST UNCERTAINTY SPECIFICATION

3.1 Introduction

The ARTIST ionogram autoscaling software is an intelligent system that UMLCAR developed for the extraction of ionospheric specification data from digisonde ionograms. There is a long-standing need to enhance the ARTIST algorithm in order for the assimilative ionospheric models such as the GAIM [Schunk et al., 2004] to know the uncertainty (*i.e.*, error bars) associated with the ARTIST-derived true height $N(h)$ -profiles. Previous efforts at UMLCAR were directed towards the development of a sensible technique for automatic calculations of the profile uncertainty boundaries. In the current project, the developed methodology is being implemented in the operating digisonde software. We also concentrated on development of novel pre-assimilation solutions that would help rule out ARTIST results that are deemed to be of low quality.

3.2 Approach

To determine the uncertainty of the $N(h)$ profiles, we constructed “boundary” profiles giving the inner and outer limits for each $N(h)$ point calculated by the NHPC inversion algorithm [Reinisch and Huang, 2001]. Figure 9 illustrates this approach.

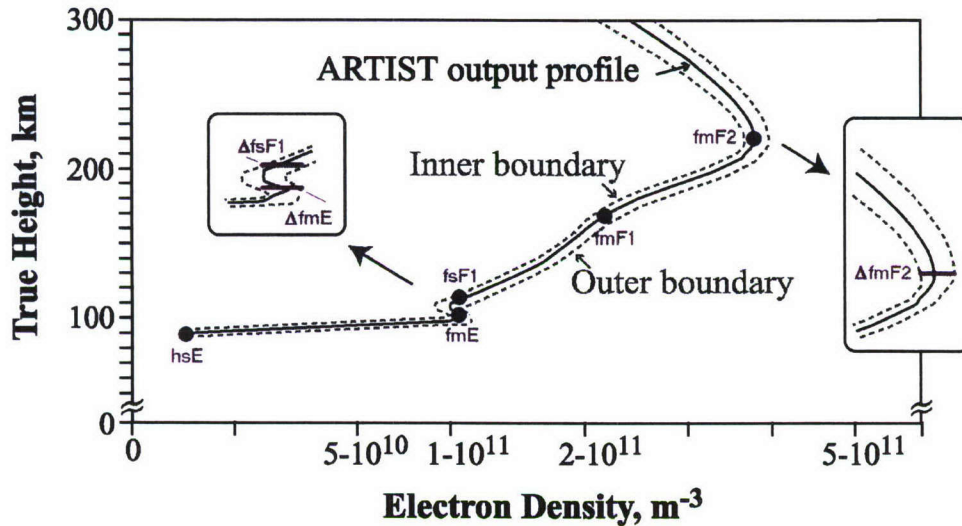


Figure 9. Point-by-point uncertainty of the ARTIST electron density profile is obtained by calculating inner and outer boundaries enclosing the profile. Both boundaries rest on five anchor points whose uncertainties are known from statistical analysis of manually evaluated differences between automatically and manually scaled values.

The inner and outer boundary profiles are determined using a set of anchor points whose uncertainties are known from statistical analysis of prior data. Figure 9 shows the profile anchor points h_sE (starting height of E layer), f_oE (plasma frequency at the E layer peak), f_sF1 (plasma frequency at the start of the F1 layer), f_oF1 (plasma frequency at the F1 layer peak), and f_oF2 (plasma frequency at the F2 layer peak).

The anchor point uncertainties vary with time, location, state of the ionosphere, and operational state and configuration of the sounder. It is, however, possible to capture the essence of measurement uncertainties through statistical analysis. Therefore, we have been concentrating our efforts on the statistical representation of ARTIST errors by comparing ARTIST results to manually interpreted “ground truth” data.

3.3 Statistical Analysis of ARTIST Performance Against Manual Data

3.3.1 General Approach

We expected that, statistically, ARTIST uncertainty would be different for different digisonde locations, geophysical conditions (such as severity of ionospheric disturbance), solar cycle, as well as with time of day and season. Thus, we envision a table of typical uncertainties for each digisonde that ARTIST software would use to find the appropriate values, depending on certain classification criteria, and then apply them to describe the derived $N(h)$ -profiles. The lookup criteria have to be determined automatically by the ARTIST itself. Obvious candidates that were considered for classification of the ARTIST results into different uncertainty groups were the ARTIST version, digisonde location and model, hour of day, season, and severity of spread F. Of all these criteria, the spread F severity level is determined using an intelligent processing algorithm, while other classification criteria such as time of day and season are stated as measurement attributes.

3.3.2 Spread F Detection Algorithms

Figure 10 shows an ionogram recorded at Jicamarca on November 22, 1998 05:00UT during severe spread F conditions (left); the right panel of 10 shows the “edge element” (edgel) pattern calculated using the assumption that every positive amplitude gradient in the mixture of overlapping echoes is a true leading edge of an echo.

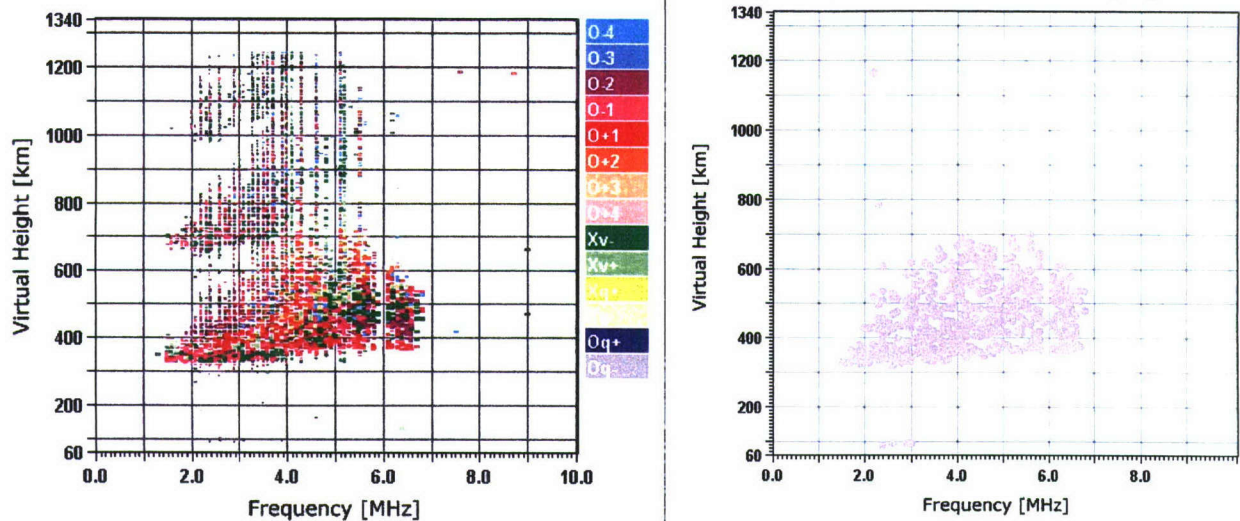


Figure 10. A digisonde ionogram recorded during severe spread F conditions in Jicamarca, Peru (left). If multiple echoes are resolved and presented as individual edgels (right), the trace extraction algorithm is overwhelmed with numerous possibilities of grouping edgels to traces.

In the ARTIST-5 software, the severity of spread F is evaluated as part of an ionogram pre-analysis by simply counting the number of edgels per frequency in the F region (see Figure 10). We use an M -criterion, where M is a median of $\{M_i\}$ and M_i is number of edgels found on frequency i , $M_i > 0$. Table 1 provides ranges of the M -criterion used in ARTIST-5 to identify four categories of the spread F conditions. ARTIST 4 and 4.5 do not have the M -criterion, but they autoscale two standard spread F characteristics, FF (frequency spread) and QF (range spread). Ranges of FF and QF for the same four categories are also given in Table 1.

Table 1. M -Criterion Values for Four Categories of the Spread F Condition

	Quiet	Moderate	Severe	Very Severe
ARTIST-5: M -criterion	< 4	Between 4 and 6	Between 7 and 11	> 11
ARTIST-4,4.5,5: FF and QF values	FF < 0.1 MHz QF < 5 km	FF < 0.6 MHz QF < 20 km	FF < 2.0 MHz QF < 70 km	FF > 2.0 MHz QF > 70 km

3.3.3 ARTIST Confidence Level of Autoscaling and Uncertainty

We are still not sure whether the ARTIST's Confidence Level of Autoscaling (CLA), an intelligent merit check of the ARTIST processing results, can be used to alter typical uncertainty bounds before they are applied to the output data. Our initial impression is that the CLA utility to spot obvious autoscaling blunders is well established, and that this capability should be used to

rule out those autoscaled records completely instead of letting them enter the assimilation process even using a high uncertainty. The ability of CLA to reliably reflect minor mistakes of the autoscaling analysis is yet to be established.

3.3.4 Calculating Uncertainty Bounds

Two major methods to deduce ARTIST uncertainties were used in the course of our study. A quick estimate of the overall uncertainty can be obtained using a cumulative difference plot, as shown in Figure 11.

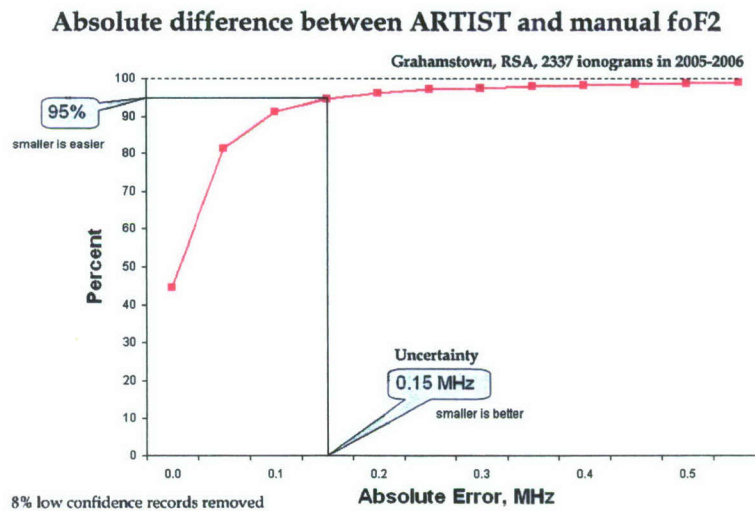


Figure 11. Cumulative difference function of the absolute |autoscaled-manual| differences for a rapid evaluation of ARTIST uncertainty. ARTIST-5 reports of foF2 for Grahamstown have 0.15-MHz uncertainty at 95% level.

The cumulative difference plots show the percent of ionograms with absolute errors less or equal to the abscissa value; they approximate the cumulative probability distribution function. The uncertainty is determined at a particular percentile; the example given in Figure 11 shows that 95% of all ionograms have foF2 errors of 0.15 MHz or less.

A more informative uncertainty estimate uses frequency histograms that treat positive and negative errors separately, as in Figure 12.

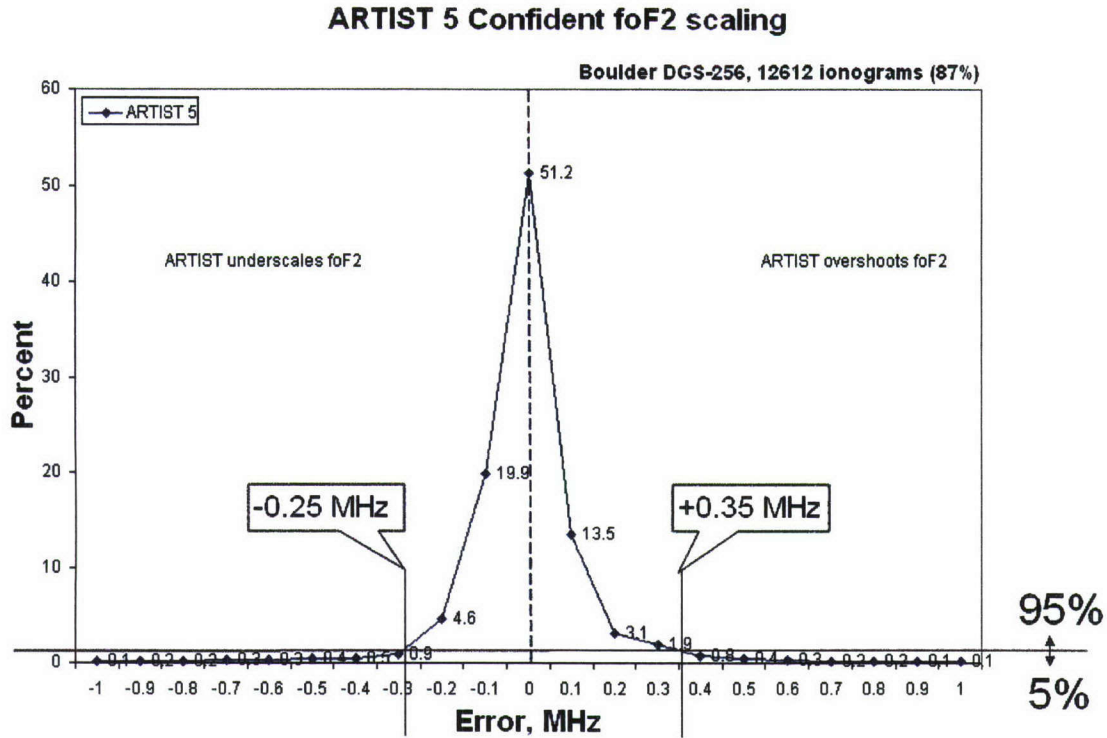


Figure 12. Uncertainty bounds for foF2 derived from the frequency histogram of (ARTIST-manual) differences for Boulder Digisonde 256 ionograms. For 12,612 ionograms scaled with confidence (87% of total 14,501 ionograms), the uncertainty bounds at 5% percentile are -0.25 and +0.35 MHz.

The uncertainty bounds were derived from the frequency histograms of (ARTIST-manual) differences at intersections of the histogram plot with the line that divides all distribution to 95% and 5% of the total ionogram count (5% percentile uncertainty). In the Figure 12 example, the uncertainty bounds are derived as -0.25 and +0.35 MHz.

3.3.5 Boulder Digisonde Dataset

We began analysis of the $N(h)$ -profile anchor point uncertainties with the dataset from the Boulder digisonde for which we have accumulated almost two years of manually interpreted ionograms. Figure 13 presents manually scaled foF2 values for the Boulder site during 2004-2006. Anchor point uncertainties were evaluated from this massive amount of data. The confidence level reflects the complexity of the ionogram (ionospheric tilt, blanketing Es, absorption, etc.) as well as the ionogram's quality.

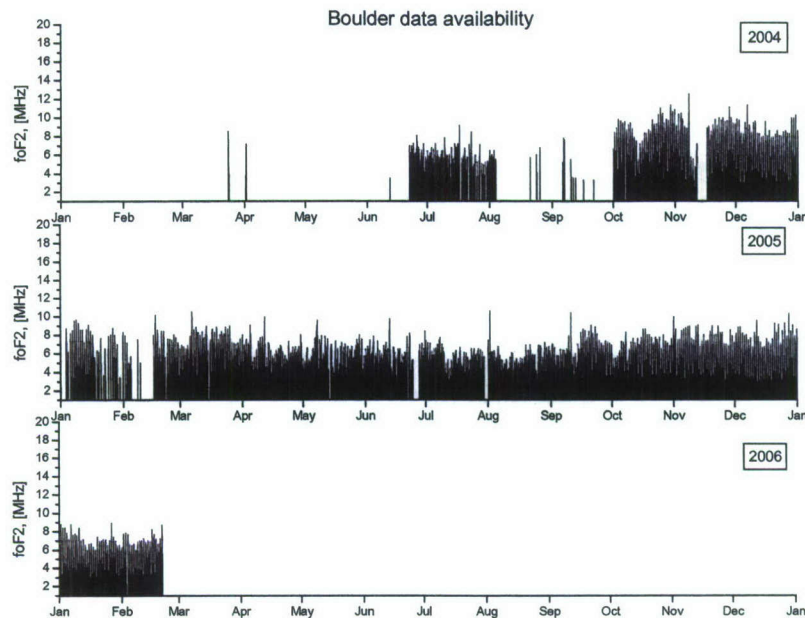


Figure 13. Availability of manually interpreted data for the Boulder Digisonde station. The plot shows foF2 for every processed ionogram for years 2004-2006.

As a first step in our analysis, the Boulder ionogram measurements were divided into two groups: one for the winter period and one for the summer period. Then, within each period, the uncertainties for nighttime and daytime ionograms were calculated. We then deduced the ARTIST uncertainty using the cumulative difference characteristic representing the difference between the ARTIST and manually scaled foF2 parameter for the same ionogram. Figure 14 shows the results of the uncertainties calculation for 46,226 Boulder digisonde ionograms scaled by ARTIST 4.5. Plots show foF2 cumulative differences calculated for nighttime and daytime ionograms for each period. The initial results show that ARTIST foF2 uncertainty (determined at 90% cumulative difference level) is equal to 0.31 MHz during the wintertime measurements with insignificant difference between nighttime and daytime measurements, and 0.17 MHz for summertime measurements, again with a small difference between nighttime and daytime ionograms.

3.3.6 Classification by Spread F Severity Level and CLA

A comparison study is underway to confirm the feasibility of detecting the level of spread F in ionograms by ARTIST-5 in order to apply different sets of uncertainty bounds to reported data. Figure 15 presents an example of such a statistical study on manually scaled Gakona, AK, DPS-4 digisonde data. It is clear from the figure that, indeed, automatically calculated level of spread F for each ionogram can be efficiently used as the criterion for associating typical uncertainty bounds on the ionogram-derived data. In this example, comparing ARTIST 5.0.2-b7 scaled foF2 values to manually interpreted values, the 95% uncertainty bound (*i.e.*, the foF2

autoscaling error value that only 5% of all processed data exceed) is 0.33 MHz for quiet conditions, 0.39 MHz for moderate spread conditions, and 0.6 MHz for severe spread conditions.

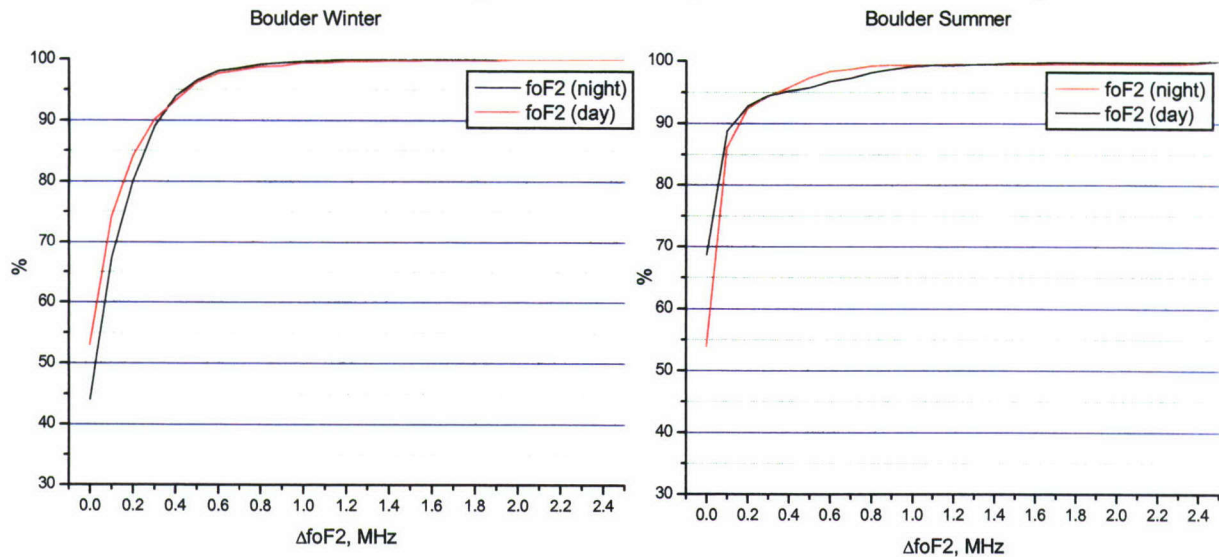


Figure 14. ARTIST 4.5 uncertainty calculated for the winter and summer time for Boulder digisonde. Plots show foF2 cumulative differences calculated for nighttime (black) and daytime (red) ionograms for each period.

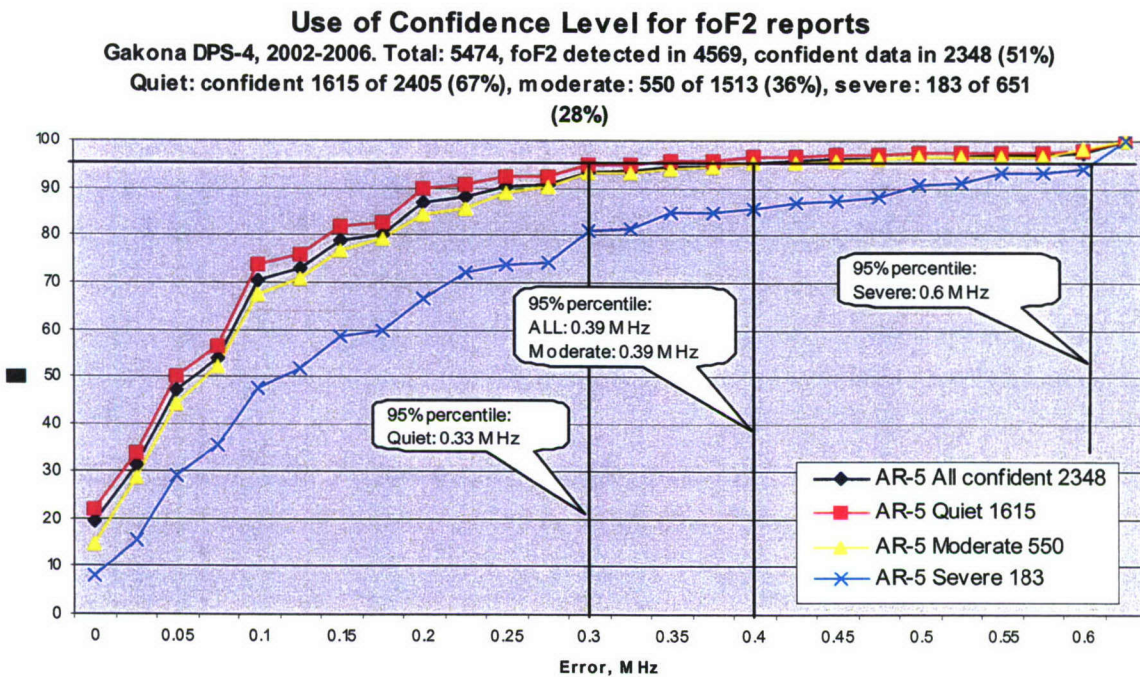


Figure 15. Uncertainty of foF2 autoscaled value for Gakona, AK, digisonde as a function of automatically detected level of spread F conditions. Comparison of ARTIST 5.0.2-b7 results for 5474 manually scaled ionograms during the 2002-2006 period.

Thus, instead of applying universally 0.39-MHz uncertainty of foF2 on all ionograms, differentiation by severity of ionospheric conditions allows a more correct report of 0.33 MHz uncertainty of foF2 for ionograms collected during quiet conditions, and 0.6 MHz uncertainty on ionograms obtained during severe spread F.

If ionograms with low confidence are removed from the analysis, the uncertainty bounds become smaller. While ~ 92% of all ionograms are scaled by ARTIST-5 confidently (CLA > 50%) at Grahamstown, interpretation at the high latitude station at Gakona, Alaska, is confident only on half of all ionograms, with only 28% of the ionograms processed confidently during severe spread F conditions.

3.3.7 Uncertainty Associated with Different Versions of ARTIST

Figure 16 presents comparison of the ionogram processing results obtained with ARTIST4.5 and ARTIST5.0 versions of the program.

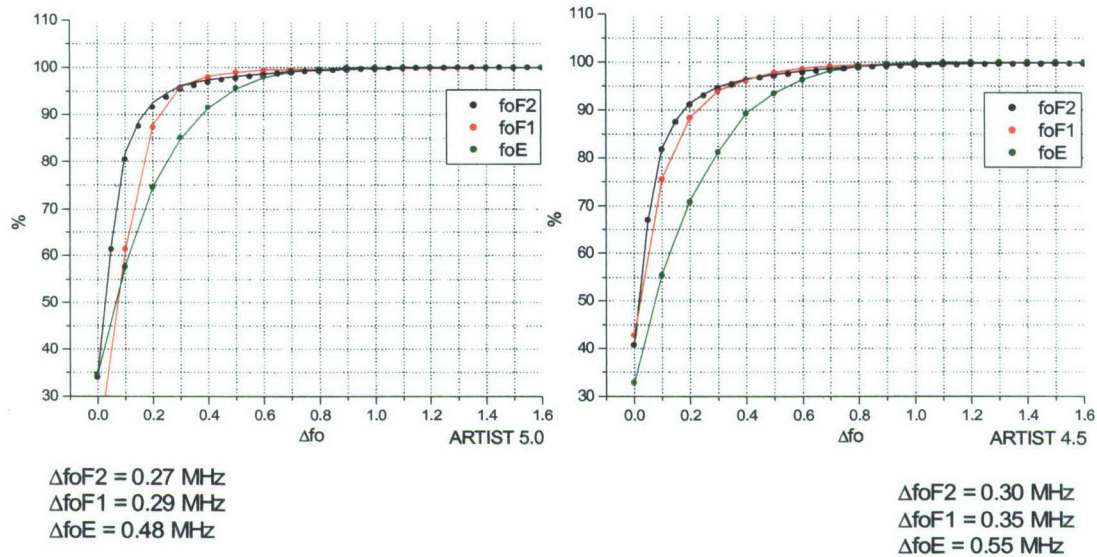


Figure 16. Cumulative difference characteristics for Boulder 2004 ionograms. This figure compares the results obtained with ARTIST5.0 (left) and ARTIST4.5 (right). Numerical values for foF2, foF1, and foE scaling uncertainties (calculated at 95% level) are listed as well.

The Boulder ionograms for the year 2004 were used as input data for this comparison. As before, the accuracy was determined as 95% uncertainty, *e.g.*, $\Delta\text{foF2} = 0.3$ MHz means that for 95% of the automatically processed ionograms, foF2 values calculated by ARTIST differ from the manually interpreted ones by less than 0.3 MHz. In the calculation of these characteristics no spread F condition detector was applied since ARTIST4.5 does not have that capability. Clearly, the latest ARTIST5.0 version provides noticeable improvement in the scaling accuracy for all three ionogram parameters. It is also worth noting that for Boulder the accuracy of foE scaling

was significantly lower than that for foF1 and foF2. This can be attributed to a higher background noise level in the lower frequency range (< 3 MHz) characteristic for that station.

3.3.8 Station-Specific Uncertainty

While we concluded that there is little uncertainty difference between day and night time ionograms, evaluations for different digisonde locations show quite remarkable station-specific differences in the ARTIST processing outcome. We performed statistical evaluation of the automatic scaling over a large amount of data collected in 2003-2004 at the following digisonde stations: Boulder, Ebro, Athens, Jicamarca, and Grahamstown. For all stations, except Boulder, the 4.5 version of the ARTIST software was used, because it is the version currently installed on those sounders. Results of the analysis are presented in Table 2 that the Boulder and Ebro stations operate the older sounder, the DGS256. These two stations also offer significantly larger amounts of manually scaled data available for the purpose of such comparison (see columns titled "Cases").

Table 2. ARTIST Uncertainty for Various Digisonde Locations

	Digisonde	Δf_oF2 , MHz	Cases	Δf_oF1 , MHz	Cases	Δf_oE , MHz	Cases
Boulder, A4.5	DGS 256	0.30	28,609	0.35	5,499	0.55	9,999
Boulder, A5.0	DGS 256	0.27	10,798	0.29	2,029	0.48	4,103
Ebro, A4.5	DGS 256	0.75	30,746	0.35	5,587	0.35	11,580
Athens, A4.5	DPS-4	0.40	6,451	0.25	455	0.25	1,124
Jicamarca, A4.5	DPS-4	0.50	6,003	0.50	948	0.35	1,999
Grahamstown, A4.5	DPS-4	0.30	2,022	0.20	348	0.20	544

The numbers in the table suggest that for the stations analyzed, the typical accuracy of foF2 and foF1 scaling is of the order of 0.2-0.5 MHz with the exception of the Ebro station. This is a very impressive result demonstrating the power of the ARTIST algorithm. For the Ebro station, for which Δf_oF1 is equal to 0.35 MHz and Δf_oF2 is equal to 0.75 MHz, the problem is the presence of a known interferer in the frequency band 6-7 MHz which often blankets a significant portion of the ionogram F2 trace near its cusp making automatic scaling extremely difficult. Therefore, the observed degraded ARTIST performance was not surprising. Note that the interferer's presence does not affect ARTIST scaling of the F1 trace which is found at a lower frequency range. The Jicamarca DPS station presents another significant challenge for an automatic processing because of the irregular nature of the equatorial ionosphere. The resulting uncertainty of 0.5 MHz reflects the complicated ionogram pattern found there. In the next step we will investigate the effect of applying the spread F condition detector algorithm to the Jicamarca ionogram processing. The accuracy of foE scaling is between 0.2 MHz and 0.5 MHz, which is a large error given the significantly smaller absolute value of foE. We are currently exploring several ways for improving ARTIST's performance in the E region.

Our main results of the ARTIST accuracy analysis accumulated thus far can be summarized as follows:

- Statistically, ARTIST does an excellent job (see Table 2).
- There is no pronounced seasonal dependence of ARTIST precision.
- Station-to-station variability of the ARTIST accuracy is significant because of the differences in the noise (interference) environment at the stations and levels of complexity of the ionogram trace signatures.

3.4 Reporting Uncertainties in SAO Format

A major effort is underway to report uncertainty bounds in the output files of the ARTIST5 autoscaler. We have been successfully using new SAOXML 5.0 format for the ionogram-derived data [<http://umlcar.uml.edu/SAOXML/>] for over two years. So far, SAOXML 5.0 is used to report the same amount of data as in previous version of SAO 4.3. The UMLCAR software is being modified to read and write uncertainty information in SAOXML 5.0.

Conceptually, only the ARTIST software currently has the capability to add uncertainty bounds to the results of its ionogram analysis. Modifications to SAO Explorer, DigisondeLib library, and the ionogram visualization routines were therefore limited to reading/writing, internal organization, and proper display of the uncertainty data. The ARTIST5 software has algorithms for calculating all necessary boundaries from the typical uncertainty bounds for the anchor points of the profile. As soon as ARTIST5 software is modified to access typical uncertainty bounds individually for each sounder location and level of ionospheric disturbance, the pipeline of automated uncertainty reports for the digisonde data will be complete.

3.4.1 Uncertainty Bounds for N(h) Profiles

Two styles of presenting uncertainty bounds for the Ne electron density profile were identified. First, each tabulated profile point can be associated with the appropriate lower and upper bounds of the reported electron density obtained from the internal and external boundaries of the profile. Second, both inner and outer boundaries can be stored analytically in terms of the shifted Chebyshev coefficients representing the boundary. While we are trying to establish contact with the GAIM experts at Utah State University to identify the preferred style of reporting the boundaries, both techniques are implemented in the SAOXML 5.0, at the expense of certain increase in the output file size. The overhead of dual reporting of the uncertainty bounds for No profile is considered at this time insignificant, considering the overall miniscule amount of the ionogram-derived data per ionogram measurement, by contemporary data archival criteria.

3.4.2 Software Modifications

Modifications to the SAO Explorer, DigisondeLib, and visualization libraries to support data uncertainties are completed and tested. Slight modifications to the standard DTD schema of SAOXML 5.0 were necessary to allow storage of the uncertainty bounds in the form of profile

coefficients. Figure 17 shows the SAO Explorer Ionogram panel displaying the profile uncertainty boundaries calculated for the Boulder ionogram taken on October 6, 2005, 19:45 UT.

3.5 Future Efforts

While the SAOXML 5.0 format has been confirmed and tested as the vehicle for delivering the ARTIST uncertainty information to the GAIM, it remains to be reviewed and accepted by the GAIM community. The review process may result in software modifications.

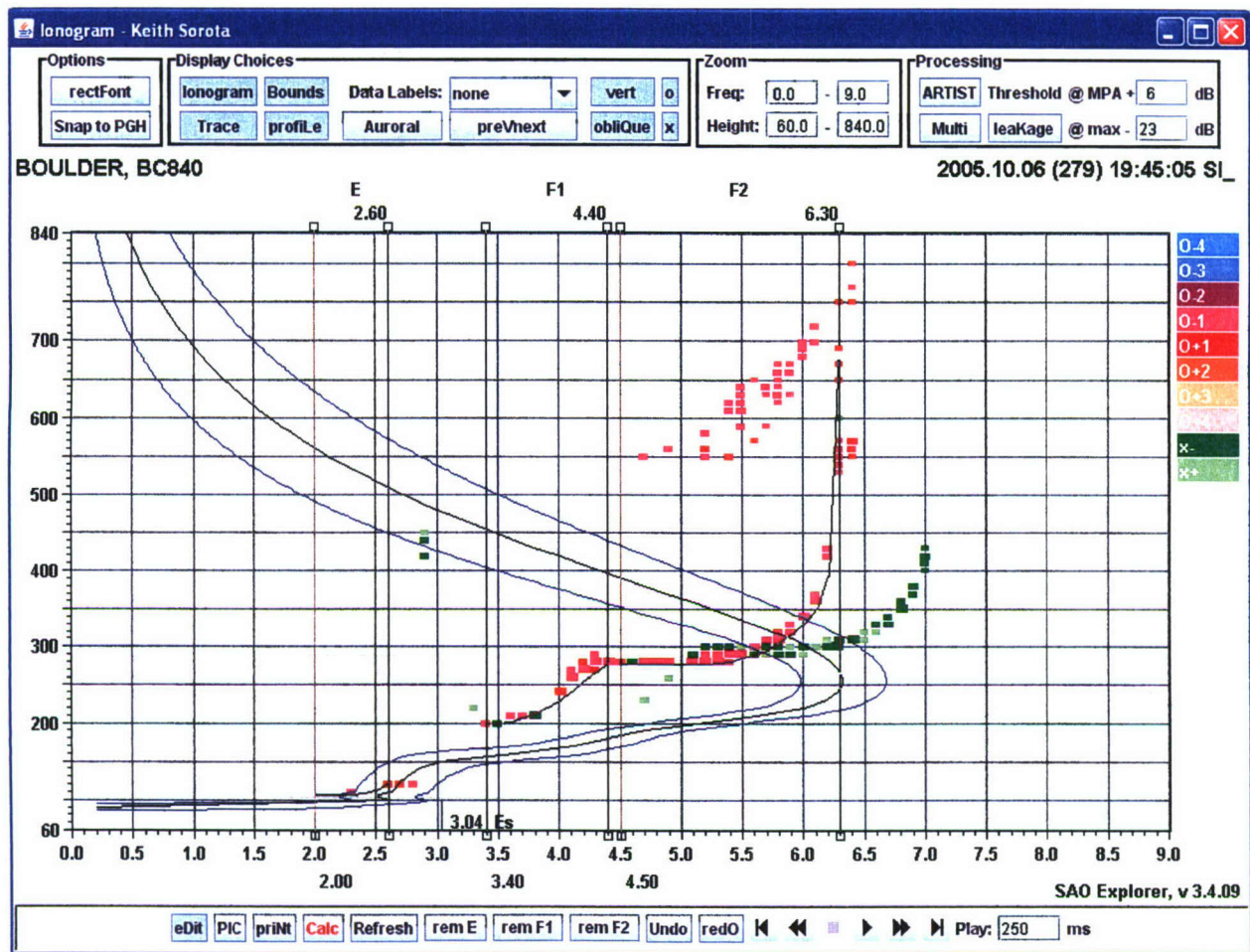


Figure 17. Calculated Profile Uncertainty Boundaries Shown in the SAO Explorer.

The feasibility of using a spread F severity detector to adaptively select uncertainty bounds for the reported ARTIST characteristics has been proven. Additionally, ARTIST5 needs to be modified so as to use an external configuration file to obtain typical uncertainties for a particular location and apply them to the output data.

The task of determining uncertainties via statistical analysis of the autoscaled versus manually scaled ionograms remains a labor-intensive undertaking. Our work on ARTIST analysis will

continue into the next year on this project. We will concentrate on developing more sophisticated confidence level detectors that will make it possible to categorize the ionograms based on their difficulties of scaling. This, in turn, will allow deducing the associated measurement accuracy for the most representative types of ionograms.

4. DIGISONDE GROUND-TRUTH DATA FOR THE NWRA TOMOGRAPHY VALIDATION PROJECT

UMLCAR continued to supply ground-truth manually verified foF2 and hmF2 values to support North West Research Associates, Inc. (NWRA) efforts to validate their TEC-based tomography calculations from GPS receiver data. The manual foF2 and hmF2 values are derived from the digisonde ionograms acquired at the Gakona and College sites during 2001-2006.

Table 3 describes the current state of the dataset acquisition and processing. The total number of manually scaled ionograms for this project is 15,613.

Table 3. Current State of Digisonde Data Acquisition and Processing for NWRA GPS Tomography Project

		Year 2001											
		J	F	M	A	M	J	J	A	S	O	N	D
Gakona		E	E	E	E	E	E	E	E	E	E	E	E
College		E	E	E	E	E	E	E	E	E	E	R	R

		Year 2002											
		J	F	M	A	M	J	J	A	S	O	N	D
Gakona		E	E	E	E	E	E	E	E	E	E	E	D
College		E	E	E	E	E	E	E	E	E	E	E	D

		Year 2003											
		J	F	M	A	M	J	J	A	S	O	N	D
Gakona		E	E	E	E	E	E	E	E	E	D	D	D
College		E	E	E	E	E	E	E	E	E	D	D	D

		Year 2004											
		J	F	M	A	M	J	J	A	S	O	N	D
Gakona		E	E	E	E	E	E	E	D	D	D	D	D
College		E	E	E	E	E	E	E	D	D	D	D	D

		Year 2005											
		J	F	M	A	M	J	J	A	S	O	N	D
Gakona		E	E	E	E	E	D	D	D	D	D	D	D
College		E	E	E	E	E	D	D	D	D	D	D	D

		Year 2006											
		J	F	M	A	M	J	J	A	S	O	N	D
Gakona		E	E	E	E	E							
College		E	E	E	E	E							

R	Request for digisonde data generated by NWRA
D	+ Digisonde data acquired in DIDBase
E	+ Edited data reported to NWRA

Total ionograms scaled by 1 September 2007: **15613**

5. PRECISION GROUP HEIGHT MEASUREMENTS OF E LAYER VIRTUAL HEIGHTS

5.1 Introduction

In the frame of the present project, we started work on the development and implementation of a routine phase measuring technique for improved virtual height measurements. Since the development of the first ionospheric sounders, there have been constant efforts aimed at

improving the accuracy of the measured characteristics of the ionosphere. Improved virtual height accuracy not only improves the accuracy of the vertical electron density profiles, but is also important for monitoring the dynamic processes in the ionospheres: tides, gravity waves, sporadic layers, neutral wind effects, etc. It is known that the characteristic vertical spatial scales of such processes range from 100 m to several kilometers. Therefore, in order to investigate these phenomena, an adequate height accuracy is essential. We focused on the virtual height of the E layers where the interaction between the neutral atmosphere and ionosphere is the most significant. Dynamic coupling from the lower atmosphere via tides and waves plays an important role in the dynamo region, where energy is injected during geomagnetic storms and then transferred to the higher heights in the ionosphere.

For an ionosonde, two major parameters characterize the accuracy of the measurements: frequency resolution and time delay accuracy. Frequency resolution is simply determined by the frequency step size selected by the digital ionosonde to scan through the ionogram and in principle can be set to any desired value. Usually it is chosen to be 20-100 kHz, which in most cases is sufficient for determining the features of the ionospheric electron density profile. Determining the exact echo delay time is more complicated. As in any radar system the digisonde measures the time of arrival of the echo pulse in relation to the time of transmission of the pulse. The pulse delay time τ is then converted to the group or virtual height h' equal to $c\tau/2$ where c is the free-space speed of light. The virtual height $h'(f)$ can then be inverted to the true height using existing true height inversion algorithms, *e.g.*, the Digisonde's NHPC program (Huang and Reinisch, 1996). Obtaining an accurate profile requires accurate $h'(f)$ values. The usual ionosonde technique of finding τ from the amplitude signature of the echo pulses has a limited accuracy of several kilometers, typically 5-10 km. The digisonde's phase technique, discussed below, which is available in each digisonde but rarely applied because ARTIST is not yet trained to make use of the phase measurements, provides an unprecedented accuracy of less than 1 km in measuring $h'(f)$.

5.2 The Virtual Height Phase Technique

The technique for measuring the range of the signal reflection using the phase difference between two separated frequencies is often referred to as the $d\phi/df$ method [Reinisch, 1996; Reinisch et al. 1997; Haines, 1994; Bibl and Reinisch, 1978]. Making use of the phase information carried by the returned signals allows significant improvement in the accuracy of ionosonde sounding in comparison to the conventional time delay methods [Davies, 1990]. The principles of the $d\phi/df$ method in a free space medium are straightforward, but in ionospheric plasma the situation becomes more complicated. This section provides the phase relations for the signals propagating in an ionized plasma characterized by its refractive index $n(\mathbf{r}, \omega)$, which is a function of position \mathbf{r} and signal frequency ω . For bottomside ionospheric sounding, the external magnetic field \mathbf{B} can be considered constant with height. We start with the eikonal solution for plane waves in a slowly varying stratified medium:

$$E(\mathbf{r}, t) = E_0 e^{-i\left(\omega t - \int_{h_0}^{\mathbf{r}} \mathbf{k} \cdot d\mathbf{r} - \phi_0\right)} \quad (1)$$

For the case of vertical propagation, we can replace r by h :

$$E(h, t) = E_0 e^{-i\left(\omega t - \int_{h_0}^{h_R} k dh - \phi_0\right)} = E_0 e^{i\phi}$$

$$\text{where } \phi = -\left(\omega t - \int_{h_0}^{h_R} k dh - \phi_0\right) \quad (2)$$

$$= \int_{h_0}^{h_R} k dh + \phi_0 \quad \text{for } t=0,$$

where h_0 stands for the height at which the signal is emitted, *e.g.*, $h_0 = 0$ for groundbased sounding. It is important that in transmission, $\partial\phi_0 / \partial\omega = 0$, and digisondes are designed to satisfy this condition. Using the relation $k = \omega \cdot n(h, \omega) / c$ (c is the speed of light in vacuum), equation (2) is recast as:

$$\phi_{rec}(\omega) - \phi_0 = \int_0^{h_R(\omega)} k dh = \frac{2}{c} \int_0^{h_R(\omega)} \omega \cdot n(h, \omega) dh \quad (3)$$

with $h_R(\omega)$ denoting the height of the signal reflection. Differentiating this equation with respect to the frequency we arrive at the following relation:

$$\frac{d\phi_{rec}}{d\omega} = \frac{2}{c} \int_0^{h_R} n dh = \frac{2}{c} h'(\omega). \quad (4)$$

Here, $h'(\omega)$ is the virtual reflection height as a function of sounding frequency. That allows us to express the phase difference $\Delta_\omega \phi$ between two frequencies ω_1 and ω_2 as:

$$\Delta_\omega \phi = \int_{\omega_1}^{\omega_2} \frac{d\phi}{d\omega} d\omega = \int_{\omega_1}^{\omega_2} h'(\omega) d\omega \quad (5)$$

Using the mean value theorem, one obtains:

$$\Delta_\omega \phi = \int_{\omega_1}^{\omega_2} h'(\omega) d\omega = \frac{2 \Delta\omega}{c} h_i' \quad (6)$$

with $h'(\omega_1) < h_i' < h'(\omega_2)$, from where it follows that

$$h_i' = \frac{c}{4\pi\Delta f} \Delta_\omega \phi \quad (7)$$

This expression makes it possible to determine the reflection height h_i' using the phase difference $\Delta_\omega \phi$ obtained from the simultaneous sounding at the frequencies ω_1 and ω_2 . There are a couple of complications, however. In actual ionospheric sounding it is not possible to directly measure the total phase of the signal, since the measured phase always contains an unknown number of multiples of 2π . Taking the 2π ambiguity into account, equation (7) can be written as:

$$h_i' = \frac{c}{4\pi\Delta f} \Delta_{\omega} \phi = \frac{c}{4\pi\Delta f} (\Delta_{\omega} \phi_{meas} + 2\pi m) \quad (8)$$

or

$$h_i' = \frac{c}{2\Delta f} m + \frac{c\Delta_{\omega} \phi_{meas}}{4\pi\Delta f}, \quad (9)$$

where $\Delta_{\omega} \phi_{meas}$ is the actual measured phase difference (which is always in the interval $0 \leftrightarrow 2\pi$), and m is an unknown integer multiplier. This 2π ambiguity in the phase measurements leads to the ambiguity in determining the range of the reflection from phase measurements alone. It is easy to see from (9) that the ambiguity $\Delta h'$ in the range measurement is

$$\Delta h' = \frac{c}{2\Delta f}. \quad (10)$$

In the digisonde, the frequency separation Δf is usually selected as a multiple of 5 kHz. Thus, if $\Delta f = l \cdot 5 \text{ kHz}$, with $l = 1, 2, 3, \dots$, then the 2π ambiguity is

$$\Delta h' = \frac{c}{2\Delta f} = \frac{3 \times 10^8 \text{ m/s}}{2l \cdot 5 \text{ kHz}} = \frac{30}{l} \text{ km} \quad (11)$$

To resolve this ambiguity, the group travel time τ determined from the echo pulse is used, which is always measured with an accuracy of the order of 5-10 km. This extra information is used to determine the first term in (9) while the precise virtual height h' is determined using the sum of the two terms, with the second term providing the desired precision, which can be estimated as

$$\delta h_i' = \delta \left(\frac{c\Delta_{\omega} \phi_{meas}}{4\pi\Delta f} \right) = \frac{c}{2\Delta f} \delta \left(\frac{\Delta_{\omega} \phi_{meas}}{2\pi} \right) = \frac{30}{l} \delta \left(\frac{\Delta_{\omega} \phi_{meas}}{2\pi} \right) \text{ km}$$

If we assume that $\Delta_{\omega} \phi_{meas}$ can be measured with an accuracy of better than $2\pi/32$ (which is easily surpassed given for reasonable signal-to-noise ratios), then the h' measurement precision will be at least

$$\delta h_i' \approx 1/l \text{ km} \quad (13)$$

i.e., for 5-kHz frequency separation it is better than 1 km.

Another complication involves the difference in the reflection heights $h'(\omega_1)$ and $h'(\omega_2)$ of the signals at the two frequencies. From equation (6) it is evident that h_i' is bounded by $h'(\omega_1)$ and $h'(\omega_2)$, and therefore the phase technique has a limited h' resolution resulting in an uncertainty u of $u \leq \frac{1}{2} |h'(\omega_2) - h'(\omega_1)|$. Therefore, the frequency difference $\omega_2 - \omega_1$ should not be too large. We estimated the height differences using routine ionogram recordings. For the mid-latitude ionosphere (Millstone Hill) during daytime, the figures given in Table 4 characterize the uncertainty of the precision group height measurements for signals separated by 5 kHz.

Table 4. Typical Precision Group Height Uncertainties
for the Characteristic Regions of the Ionosphere

Region	Uncertainty (5 kHz)
E	25 m
E cusp	125 m
F bottom	75 m
F cusp	750 m

The numbers in Table 4 show that the uncertainty is large only near the F layer cusp. Even at the F cusp, however, the uncertainty is smaller than 1 km

5.3 Measuring E :Layer Heights at Millstone Hill

A multi-frequency precision group height (MPGH) technique has been implemented into the DPS-4 sounder operating at the Millstone Hill Observatory. In September and November 2006, the digisonde was programmed to carry out routine MPGH measurements of E layer heights, operating in the so-called “drift mode”. In total, there were 40 days of observations accumulated with a measurement cadence of 15 minutes made in the intervals of 1 – 21 September and 31 October – 19 November 2006. The purpose of this campaign was to monitor the dynamics in the E-region and to evaluate the performance and robustness of the MPGH technique. The following four frequencies were used for sounding in the frequency-multiplexing mode: 2330 kHz, 2335 kHz, 2340 kHz, and 2345 kHz. Making use of the well-known expression relating the plasma frequency f_p and the electron density N_e ($N_e = \frac{1}{80.6} f_p^2$, where N_e is in m^{-3} and f_p is in Hz) these frequencies provided measurements at the heights corresponding to electron densities around $6.74 \times 10^{10} \text{ m}^{-3}$. Only echoes from E region heights between 90 and 135 km were considered. New software codes for automatic processing of these new measurements has been developed.

The group of four sounding frequencies produced three different frequency pairs with 5 kHz separation. For each sounding frequency we collected echoes from 18 ranges spaced by 5 km at the four antennas. After Fourier transforming the received signals digisonde software selects the strongest spectral components for processing. Only signals at least 12 dB above the noise level of a spectrogram were included in the analysis. The complex Fourier transform also gives the signal phases from which the phase differences $\Delta_{\omega} \phi_{meas}$ used in (9) were calculated. A number of tests were used to improve the reliability of the results: only signals that have similar phases on all four antennas were considered in order to discard off-vertical echoes; also, only those calculated precision group heights were included that were within 7 km of the h' value determined by the coarse time delay measurement using only echo amplitudes. Thus, for each digisonde sounding, it was possible to calculate a large number of independent precision group heights: one for each antenna, each frequency pair, each coarse range and for several of the strongest spectral lines. This made it possible to obtain a statistical distribution of measured group heights for a single observation. Analysis has shown that, in most cases, a significant majority of the calculated

group heights ($\geq 65\%$) were concentrated within a single statistical height bin 1 km wide (Figure 18).

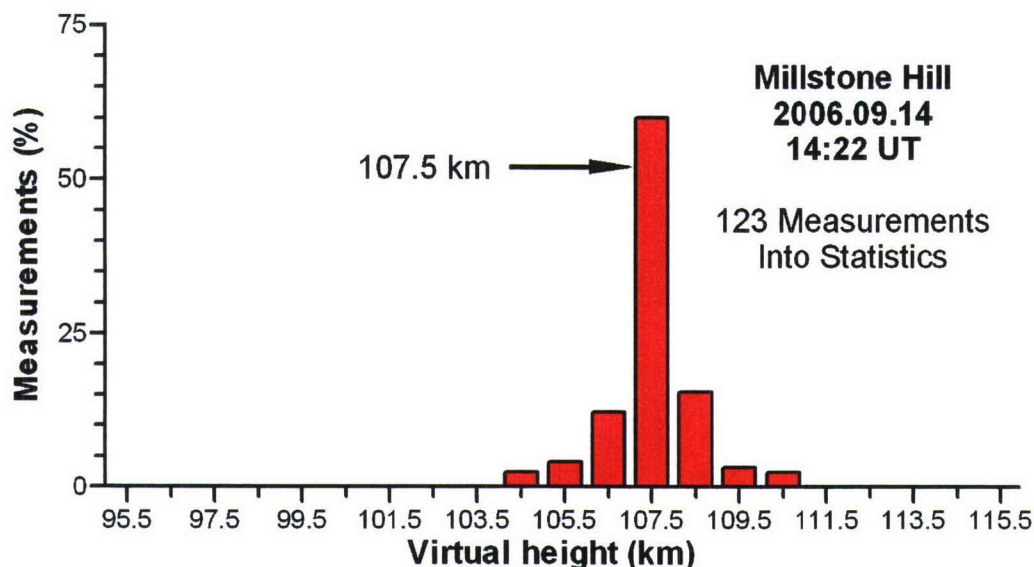


Figure 18. Distribution of virtual heights during one sounding made on 14 September 2006 at 1422 UT. A majority of the calculated heights are concentrated within a single statistical range bin at 107.5 ± 0.5 km.

Given this distribution, it seems justified to use the median as the most representative value for the precision group height. This processing algorithm made it possible to reduce a large amount of the raw sounding data to a single precision group height for each of the observation made once every 15 minutes.

Results of the MPMGH measurements carried out in September 2006 are presented in Figure 19 showing the time evolution of E layer virtual heights. Naturally, the radiowave reflections from the regular E layer were observed only during daytime. The presented data clearly demonstrates an expected daily pattern of the E region virtual height variation with a minimum height near local noon (1630 UT approximately) and apparent maximum heights at sunrise and sunset (approximately 12 UT and 21 UT respectively). For these 20 days of observations, the average daily variation is shown in Figure 20.

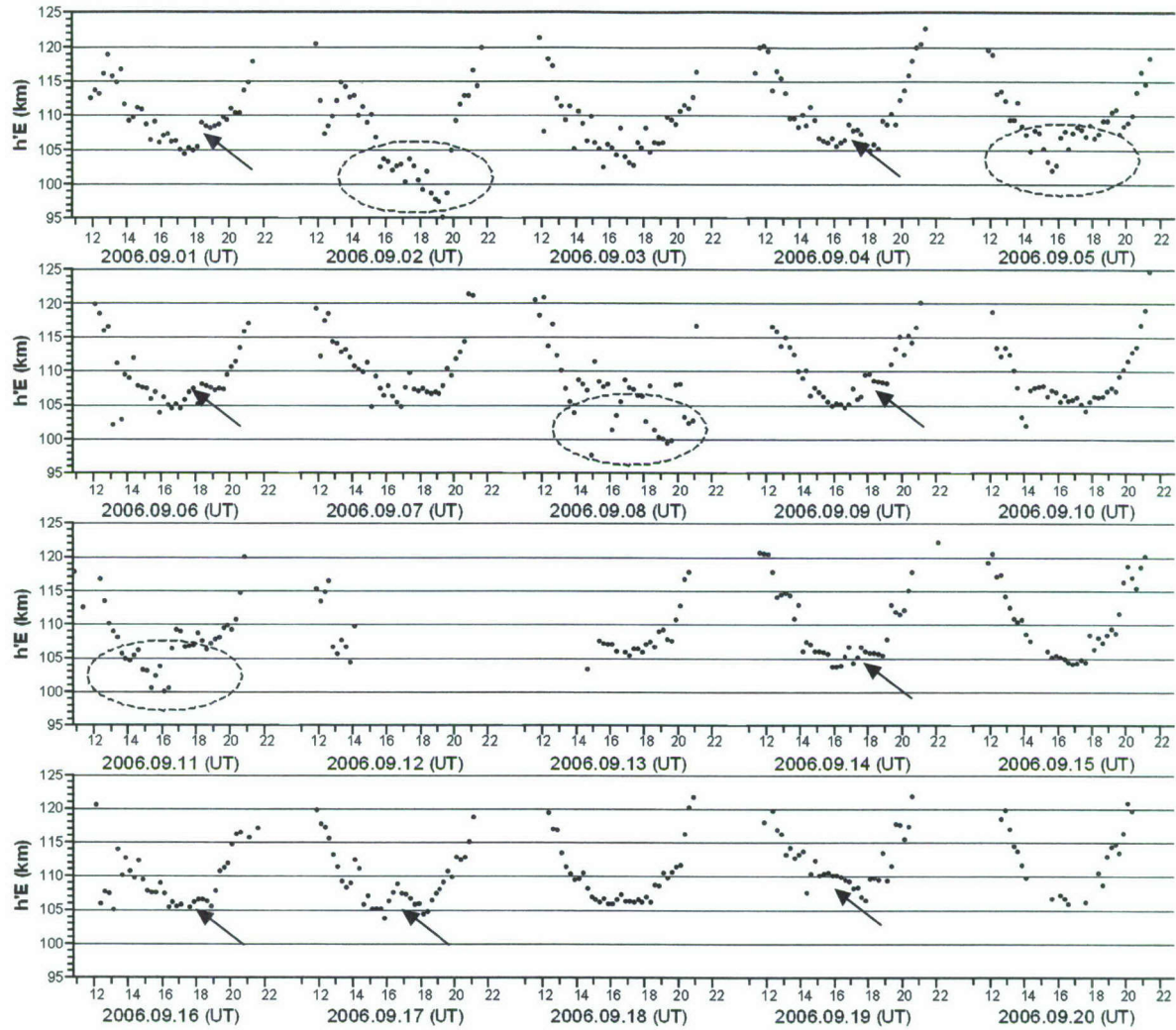


Figure 19. Daily E region precision group heights at Millstone Hill as function of time. The horizontal axes represent time (Universal Time), and the vertical axes represent virtual height (km). Dashed circles highlight significant decreases in E layer virtual heights and the black arrows point to hook-shaped disturbances.

From the monthly mean plot, one can see that after sunrise the recorded E layer virtual height was 117 km, which then decreases to 105 km at local noon, and subsequently rises back up to 122 km right before sunset. The calculated standard deviations are about 4–5 km near sunrise and sunset times, and 1.5–2 km near noontime. In addition to the monthly average pattern, it is possible to observe a day-to-day variability (Figure 20). Comparing the monthly average pattern in Figure 20 with the daily variations recorded in September 2006 (Figure 19), one notices significantly lower heights on September 2, 5, 8, and 11 (between 14–20 UT), with the measured virtual height values as low as 98 km. These features were indicated in Figure 19 with the dashed circles. The observed differences of 5–7 km between the heights measured on those days and average values are significantly larger than the standard deviations for the corresponding time interval.

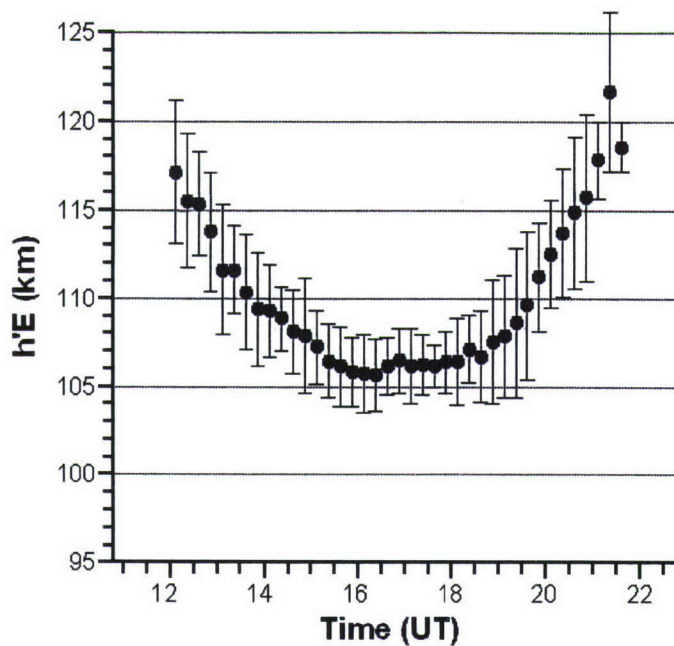


Figure 20. Average daily variations of the $h'E$ obtained from the 20 days of September. Vertical error bars indicate the standard deviation obtained at a given time.

Interestingly, these ‘low daily values’ occurred with a periodicity of three days, which could be indicative of some oscillation activity at E-region altitudes. Similar oscillations have been found in the electron density variations in the E layer by other authors. For example, Zhou [1998] reported a clear two-day modulation of the electron density at the altitude range of 84–94 km, which he attributed to quasi two-day planetary waves. The $h'E$ variations we observe in this work closely resembles height variations at fixed electron density presented in Zhou.

Results of the data analysis demonstrate the great potential offered by ionospheric sounding with enhanced height resolution. It can be concluded that in practice the height precision offered by the new method is better than 1 km. The feasibility and stability of these measurements are confirmed by the very narrow statistical distribution of the independently determined group heights for each sounding. The accumulated data made it possible to observe very interesting effects in the daily variations of the E-region heights. We were able to observe day-to-day variability, which in the case of the September measurements demonstrated an interesting three-day periodicity. This dataset also shows repetitive “hooks” in the h' records. It is important to point out that such results could not have been obtained using the conventional time delay measurements because the characteristic amplitude of these unusual variations is about one kilometer. Our preliminary study of the observed effects suggest that day-to-day variability of the E layer height variations could be related to planetary wave modulation of metallic ion transport while the “hook” variations (see arrows in Figure 19) may be caused by tidal/gravity wave activity. The existing worldwide digisonde network offers a great advantage of organizing unprecedented simultaneous observations on a global scale.

6. PROCESSING OF DIGISONDE DRIFT MEASUREMENTS

6.1 Introduction

We have been working on the analysis of ionospheric plasma drift velocity data accumulated in the DriftBase database over the last few years. A number of digisondes routinely measure ionospheric “HF drift” after each ionogram observation. It is well known [Bullett, 1994; Reinisch et al., 1998] that these high frequency (HF) drift measurements do not directly measure the ion drift, but rather give the changes in the location of ionospheric structures with time, *i.e.*, an apparent plasma drift velocity. If these ionospheric motions are controlled primarily by plasma transport processes (which is usually the case for middle- and high- latitudes), then the two velocities are equivalent. By comparing the digisonde drift velocities to the ISR measured ion drift at Millstone Hill (a mid latitude station), Bullett [1994] experimentally confirmed the validity of the digisonde drift method. The observed agreement between the two techniques was best at night and when no traveling ionospheric disturbances (TIDs) were present. Certain differences in the two velocities, however, were observed during the daytime and under non-equilibrium conditions [Reinisch et al., 1998]. In the equatorial region, this technique should provide meaningful measurements for the horizontal plasma velocity component, which is not significantly affected by chemical processes.

Currently, at most of the digisonde stations running the drift mode, the plasma drift velocities are calculated automatically with the Digisonde Drift Analysis (DDA) software package and then archived in the UMLCAR drift velocity database “DriftBase” (<http://ulcar.uml.edu/Drift-X.html>). Using statistical analysis of the available drift data we wanted to establish and understand the typical daily “plasma drift” variations as measured by the digisondes. We are interested in finding correlations between the behavior of the plasma velocity and other geophysical processes controlling the ionospheric dynamics.

6.2 Data Analysis

We started a statistical analysis of the routine F region digisonde drift measurements using data from the Ebro station in Spain (40.8°N, 0.5°E). In total, we have analyzed 18 months of the vertical (V_z) velocity component data collected during years 2004 and 2005. First, we determined the typical daily pattern in terms of the main harmonics (diurnal, semidiurnal, and terdiurnal). The sum of the first three daily harmonics reproduces the observed monthly median quite well (Figure 21), except for the deep negative excursion near sunrise. The spectral characteristics of the harmonic components have been computed from the monthly median values by a general least-square method.

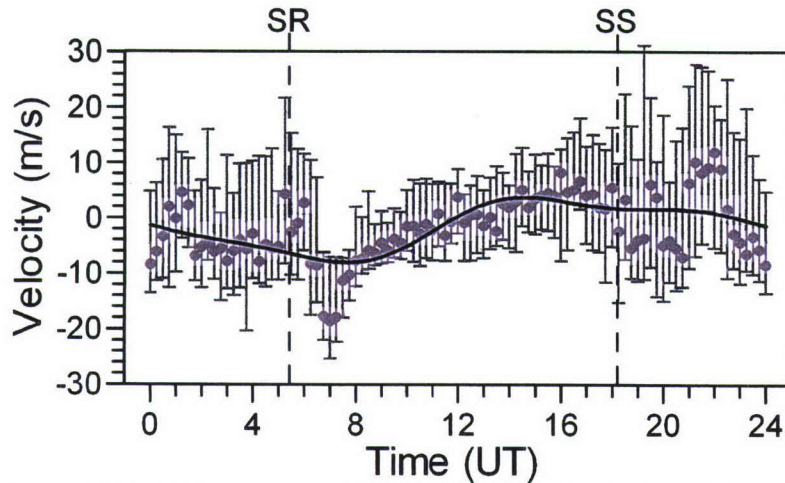


Figure 21. Daily pattern of the vertical velocity data from the Ebro digisonde for December 2004. The 15-minute median values of V_z are shown as gray dots. The vertical error bars indicate the range of 80% of V_z values for each given time. The solid line represents the daily pattern calculated as a sum of the primary diurnal harmonics. The vertical dashed lines indicate the sunset (SS) and sunrise (SR) above the station at an altitude of 300 km.

We have analyzed the daily patterns of V_z and its variability as a function of local time and season. Figure 22 presents amplitudes and phases of the three main daily harmonics as a function of season. Figure 23 shows the seasonal variation of the phase of the semidiurnal harmonic (left panel) and semidiurnal harmonic phase as a function of sunrise time (right panel). The main results are summarized as follows: (1) V_z displays larger variability during nighttime and during winter; (2) the diurnal harmonic is dominant with the larger amplitudes observed at equinox compared to that at solstice (Figure 2, left panel); (3) the amplitude of the semidiurnal variation is enhanced near equinox, while terdiurnal variation is strongest during the summer half-year (from March to September) when it has a larger amplitude than the semidiurnal (Figure 22, left panel); (4) the phases of the diurnal and terdiurnal harmonics are practically constant for the whole year (Figure 22, right panel); (5) the phase of the semidiurnal harmonic is the key parameter for matching the minimum values of the daily pattern of V_z (Figure 23, left panel) because it is sun-synchronous, *i.e.*, its variation follows the change in the sunrise time (Figure 23, right panel).

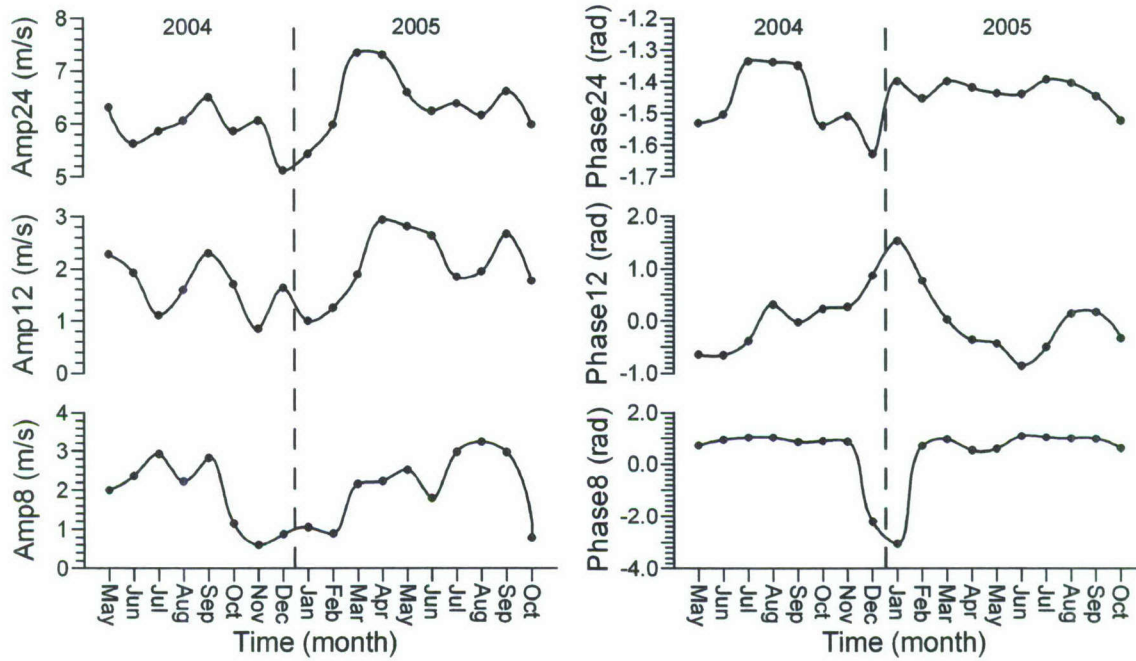


Figure 22. Seasonal variations of the amplitudes (left) and phases (right) of the daily pattern of the V_z in the F region. The top plots show the diurnal component, the middle and bottom ones correspond to the semidiurnal and terdiurnal component, respectively.

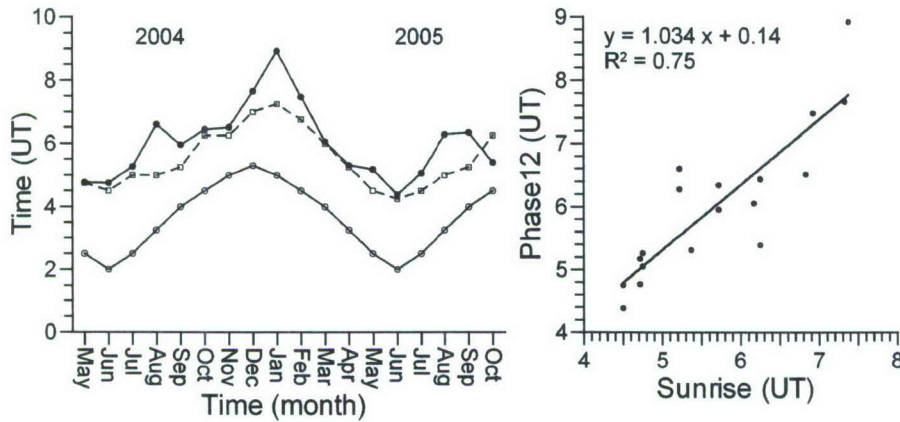


Figure 23. The left panel shows the seasonal variation of the phase of the semidiurnal harmonic (full line with full dots), the time of the minimum values of the daily pattern of V_z (dashed line with open squares) and the sunrise time at 300-km height (full line with open circles). The right panel shows the scatter plot of the semidiurnal phase against the sunrise time for a given month. Solid line is the best linear fit with the correlation coefficient indicated.

The large variability of V_z during nighttime and its winter enhancement can be in part explained by the neutral wind dynamics and auroral energy inputs. Other physical mechanisms may also account for some of the variability. According to the observed results, we believe that it is feasible to model the daily pattern of the V_z component in the F region using digisonde drift measurements. The results presented here are representative only for the Ebro station, and they are likely to vary with latitude and longitude. The formulation in terms of Fourier harmonics is quite simple (requires one parameter for each month) and is easily updateable. In addition, it is straightforward to extend this formulation to a larger geographical region by analyzing digisonde drift measurements at other latitudes and longitudes.

Larger data sets are required to test/verify a possible solar activity dependence, and to assess whether the proposed formulation is useful for global and long-term applications. Note that the formulation in terms of Fourier harmonics does not precisely capture the V_z behavior around sunrise. The typical daily pattern of V_z and its seasonal trend show larger amplitudes during equinox, agreeing with the expected seasonal pattern as predicted by the Richmond et al. [1980] using his empirical drift model (derived from ISR measurements). This also applies to the variation in the time of the maximum V_z .

The diurnal component of the V_z drift pattern is dominant, calculated using the Ebro measurements, on the other hand, the Richmond model predicts a dominant semidiurnal harmonic. This, in principle, may be a manifestation of the fact that digisonde measures an “apparent” plasma velocity, while the Richmond’s model was developed for the $E \times B$ drift. However, the daily V_z pattern that we have established in this work is an average characteristic, and therefore the effect of irregular phenomena like TIDs should not be significant. In the future, we will investigate this observed difference between the model and the measurements in greater detail. We will concentrate on the role of the neutral wind which has a systematic behavior and may effect the average vertical motion of the ionosphere at mid-latitudes. Some preliminary results of this analysis were reported in an earlier report.

Another station for which this statistical data analysis has been run is the Jicamarca equatorial station (12.0°S, 283.2°E). Figure 24 presents the averaged monthly patterns for the digisonde east-west velocity component at Jicamarca in 2006. The months are indicated on each panel. These data were processed using the Drift-Explorer software package. The monthly east-west velocity pattern is remarkably well defined and the month-to-month variability is also apparent. Error bars indicate standard deviations which are reasonably small for this kind of measurements. Positive velocity in these plots corresponds to eastward plasma flow. The change from eastward to westward direction of the plasma motion, easily noticeable on the plots, approximately corresponds to the transition from nighttime to daytime.

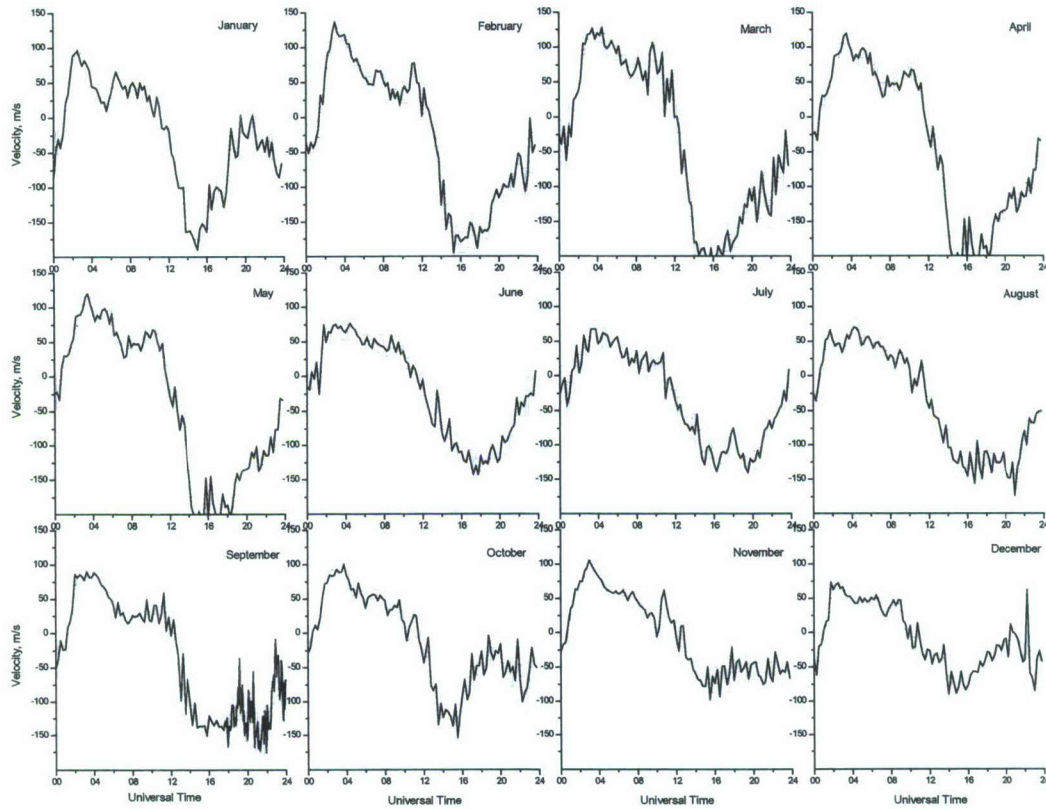


Figure 24. Monthly averaged east-west drift velocity data measured at Jicamarca station in 2006.

Figure 25 presents the results of spectral analysis of the east-west velocity, namely the monthly amplitude spectra. Not surprisingly, for all the months shown, the diurnal line is the strongest, however, occasionally the semidiurnal and terdiurnal lines are also appear. There also appears a large variability to the intensity of these harmonics.

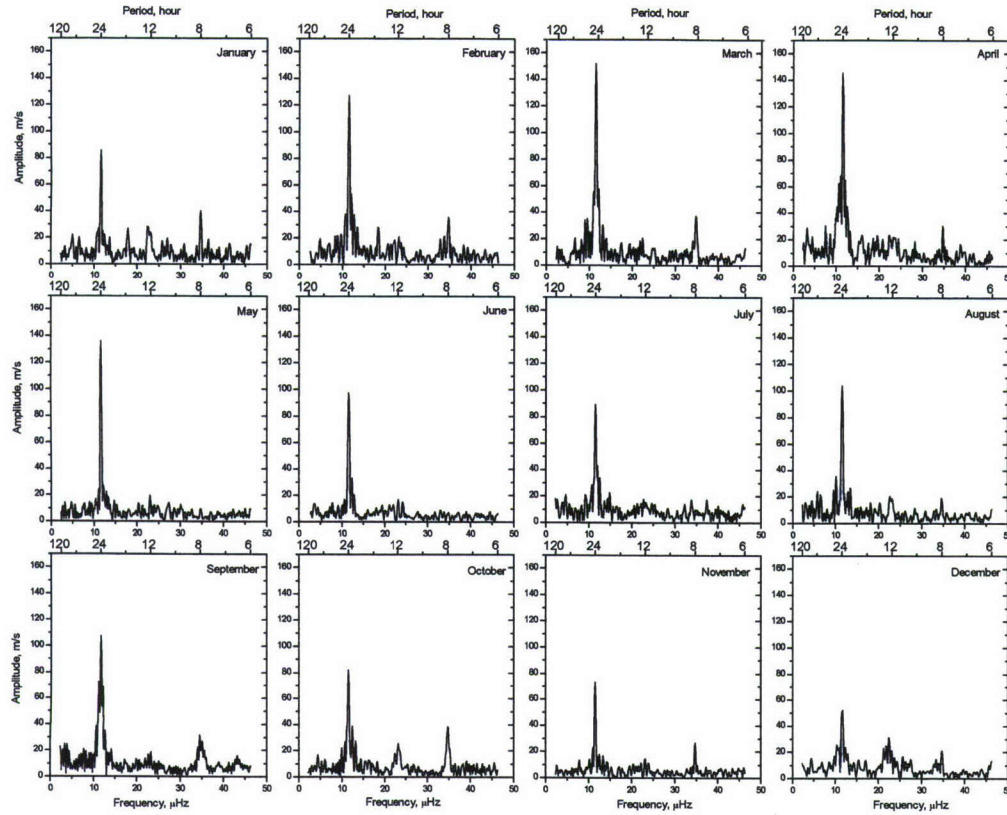


Figure 25. Amplitude spectra of the east-west plasma velocity measured at Jicamarca in 2006. Bottom axis shows the frequency in μHz while the top axis shows the corresponding time periods in hours.

In principle, we possess enough data for establishing a statistical model for the east-west plasma drift velocity at Jicamarca similar to the Richmond et al. [1980] model, however, our interest is in analysis of the physical significance of the observed variations and search for a possible correlation with other processes in the ionosphere.

6.3 Future Efforts on Drift Data Analysis

We believe that these results give evidence that the digisonde drift measurements can be used for monitoring the F region ion drift. The systematic analysis of such observations can contribute to a better understanding of the ionospheric dynamics. Our future efforts will extend this work of digisonde F region drift analysis to other digisonde locations. We plan to process more data from Jicamarca as well as from other stations using spectral analysis (as it was done for Ebro station data) in order to be able to analyze seasonal variations of the plasma drift velocity pattern and to investigate its relationship with other geophysical processes.

6.4 DDA Software Upgrade

To make the drift data processing more efficient we worked on upgrading the DDA software. A translation of the first half of the existing Fortran-based code to the Java platform is completed. A number of optimizations were made and several programming errors were corrected in the process. This is a significant step forward enabling the unification of the drift data processing algorithms with the rest of the digisonde programs and making use of the extensive library of the Java classes developed earlier. It is now possible to easily maintain and/or update these programs, a process that previously required significant time consuming efforts because of the difficulty of deciphering Fortran code. After this translation, the Drift-Explorer package has an embedded capability of calculating the skymaps from the raw drift data, which is useful for both digisonde system testing and data analysis. The second half of the DDA software involving the velocity calculation routines will be converted into Java in the upcoming year.

7. STUDY OF THE IONOSPHERIC RESPONSE TO STRONG GEOMAGNETIC STORMS

7.1 Introduction

The response of the Earth's ionosphere to strong geomagnetic disturbances is still one of the primary interests in ionospheric science [Rishbeth et al., 1996]. Geomagnetic disturbances are generated by changes in the solar wind and interplanetary magnetic field (IMF) interacting with the earth's magnetosphere. The earth's reaction to such perturbations is commonly referred to as an ionospheric storm. Typically, these storms are categorized into two characteristic types: positive storms (with the ionospheric electron density increase) and negative storms (with the electron density decrease). There is fair agreement concerning the mechanisms of the negative storms, which are attributed to the composition changes of the neutral atmosphere resulting into a faster recombination rate, thus depleting the plasma [e.g., Buonsanto 1999; Mendillo, 2006]. A more complicated story involves the positive storms. A number of different mechanisms have been suggested to explain storm morphologies but a complete picture has not yet emerged. Prölss [1993] has offered the most comprehensive description of the storm development, placing the crucial role on the neutral wind disturbances generated by heating of atmospheric gas at auroral latitudes. In his model such neutral wind perturbations are often carried to lower latitudes by traveling atmospheric disturbances (TAD) which are a superposition of atmospheric gravity waves. TADs, propagating from higher latitudes, carry along meridional winds that push the ionospheric plasma upward along the magnetic field line that in turn leads to the increase in the plasma density because of the slower recombination rate at higher altitudes [e.g., Rishbeth, 1998]. This seems to be a promising mechanism and its validity has been confirmed by global scale modeling [Fuller-Rowell et al., 1994]. However, experimental verifications are still scarce. One of the difficulties is that the measurements needed have to be made on a large spatial scale and, in addition, measurement of the height changes are also required. The problem is that most of the ionosphere measuring instrumentation either does not measure the height distribution of electron density (e.g., GPS TEC measurements), or cannot provide significant spatial extent and routine observations (e.g., incoherent scatter radars). The large number of existing ionosondes make it possible to carry out this analysis, but many sounders are not capable of automatic

calculation of the true height distribution of electron density (*i.e.*, inverting the measured virtual heights); therefore, such a task requires an unreasonable amount of time and considerable human-based processing. In this situation, an existing worldwide digisonde [Reinisch, 1996] network can provide the dataset suitable for such an investigation. It offers routine automatic round-the-clock ionospheric height profile measurements over a wide range of latitudes and longitudes. Even though manual verification of the ionogram processing is often recommended, the whole process is greatly simplified by using the available digisonde software packages.

We took advantage of the large amount of data collected over a significant period of time and ran an analysis of the mid-latitude ionospheric response to geomagnetic storms using the digisonde observations at different longitudes and latitudes. For the major storms of 2001-2005 we analyzed the evolution of the F layer making use of the electron density profiles and main ionospheric characteristics such as foF2 and hmF2. In this reported research we focused on the very strong ionospheric storm of August 24, 2004.

Table 5. Digisonde Station Coordinates

Station	Geo Coordinates (Lat; Long)	GM Coordinates (Lat; Long)
Europe		
Chilton	51.5° N; 359.4° E	53.7° N; 84.4° E
Ebro (Pruhonice)	50.0° N; 14.6° E	49.6° N; 98.6° E
Roquetes	40.8° N; 0.5° E	43.2° N; 81.3° E
San Vito	40.6° N; 17.8° E	39.9° N; 98.3° E
Athens	38.0° N; 23.5° E	36.4° N; 103.0° E
America		
Millstone Hill	42.6° N; 288.5° E	52.9° N; 0.3° E
Boulder	40.0° N; 254.7° E	48.3° N; 320.5° E
Wallops I	37.9° N; 284.5° E	48.1° N; 355.6° E
Eglin	30.4° N; 273.2° E	40.3° N; 342.9° E

Analysis was limited to the American and European sectors where there exists a dense network of sounders. Most of the time the digisonde stations operated at a 15-min cadence. Coordinates of the mid-latitude stations are given in Table 5. Unfortunately, during strong geomagnetic disturbances high latitude and polar stations often do not produce useful measurements because of strong radiowave absorption in the lower ionosphere.

7.2 Data Analysis

In Figure 26, we see the variation of the geomagnetic parameters for the strong geomagnetic storm that occurred on August 24, 2005 with storm commencement (SC) at 0613 UT. In this figure the solar wind plasma density, plasma speed, interplanetary magnetic field (IMF) components, and SYM-H index (DST index analog) are shown. The storm commencement at 0613 UT coincides with a rapid increase in SYM-H index and similar abrupt changes in IMF and solar wind parameter values.

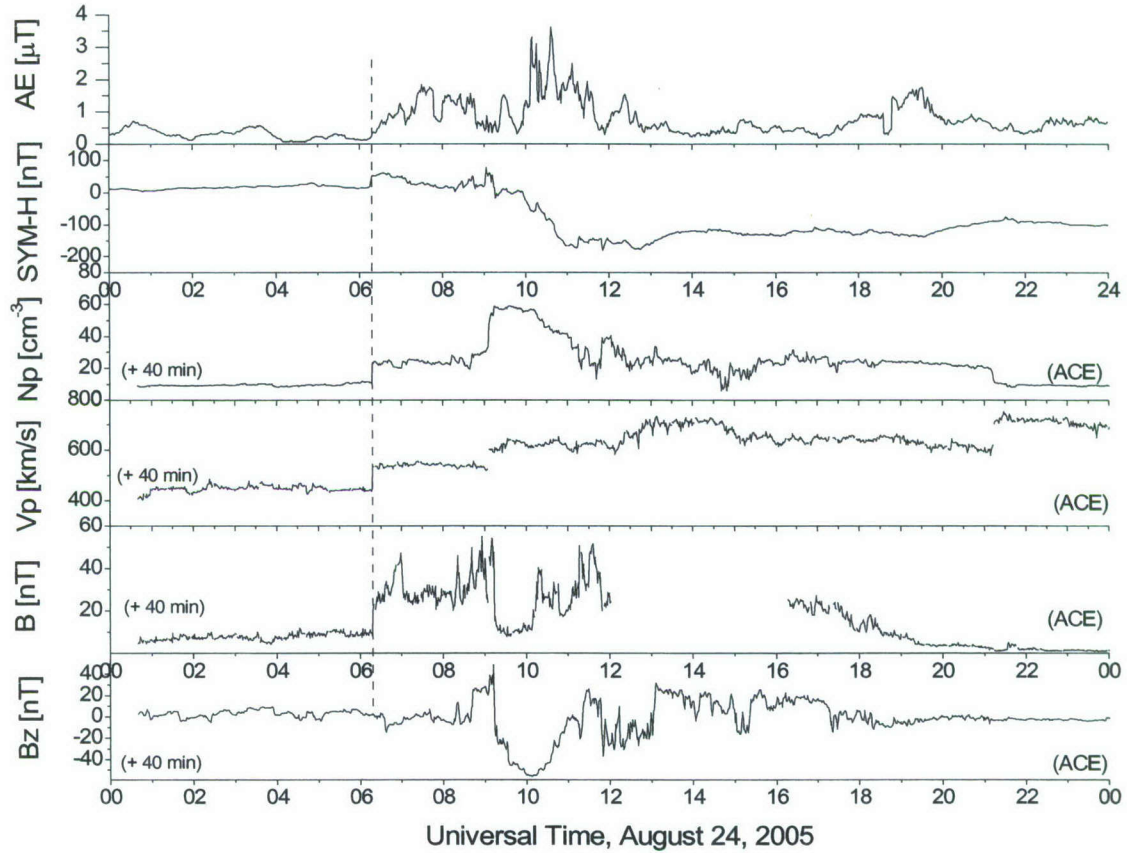


Figure 26. Geomagnetic storm of 24 August 2005. The top panel shows SYM-H index variations, and the next panels show the solar wind plasma density, plasma speed, and the last two panels show the interplanetary magnetic field components. The solar wind and IMF data were taken using the ACE satellite and were shifted by 40 minutes to account for the position of the satellite.

Note that at about 0900 UT there is another shock event accompanied by a southward turning of IMF Bz component. At about the same time the main phase of the storm begins with the SYM-H index reaching its minimum at 11 UT. The value of the minimum of -200 nT indicates a moderately strong geomagnetic storm

We first compared the ionosphere behavior on the day of the storm event to the average quiet day pattern. Figure 27 introduces variations of the ionospheric electron density height profile as a function of time. In this figure the left panels shows the average quiet day data for the European stations Chilton, Pruhonice, Ebro, San Vito, and Athens with the station locations given in Table 5. The profiles shown are plotted in terms of the true height, which is derived from the original measurements with the standard digisonde inversion routine NHPC. All of the ionogram data have been reviewed before being used in the profile calculation. The topside parts of the profiles are approximated by an α -Chapman function [Reinisch and Huang, 2001]. The plots are in

universal time, but ionospheric sunrise and sunset times are indicated for one of the stations with red and black semi-circles respectively, helping to distinguish daytime and nighttime periods.

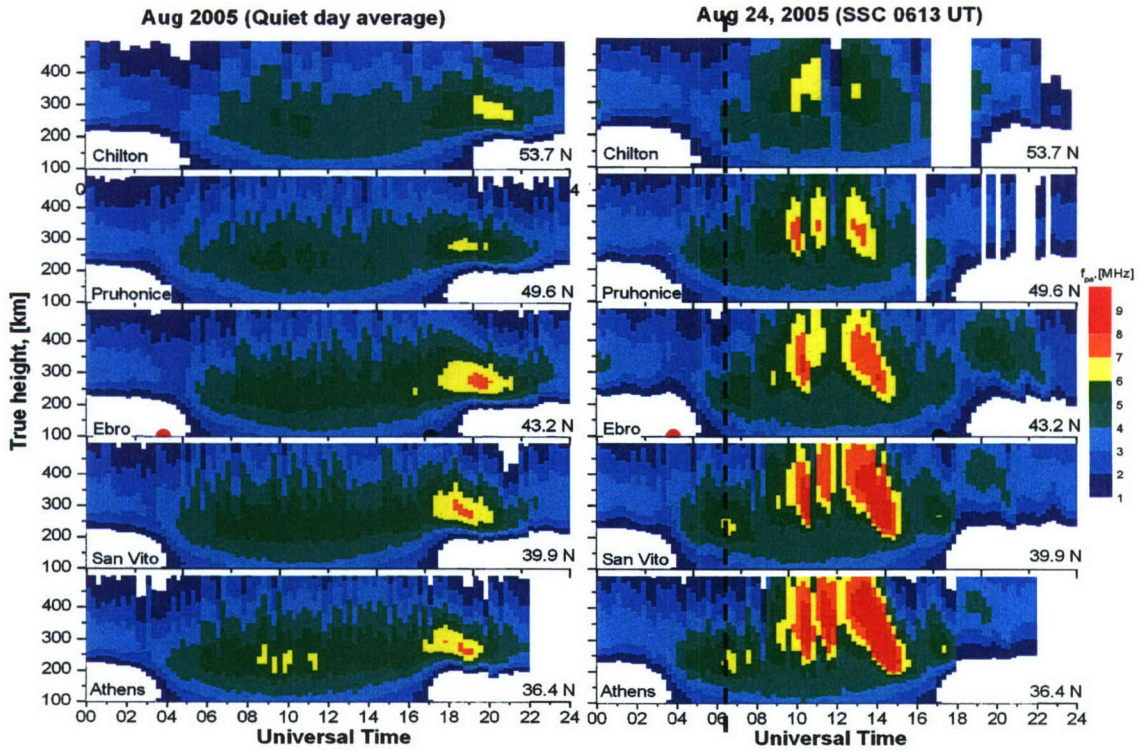


Figure 27. Electron density profile variations as a function of time for the listed European stations (see Table 5). The right panel shows storm day (August 24, 2005) data, while the left panel shows the quiet day average data. Electron density is presented in terms of equivalent plasma frequency (color bar). Sunrise and sunset times are indicated for the Ebro station with red and black circles correspondingly.

Data from the different stations are arranged according to the station's geomagnetic latitude as indicated on the plots. The quiet day pattern was calculated with the CARP (Calculate Average Representative Profile) program by averaging over height profiles for four quiet days, namely, August 17-20, 2004. The effect of the ionospheric storm, *i.e.*, the difference between the disturbed and quiet day data is quite significant. On the disturbed day a series of electron density enhancements were observed between 08 UT and 15 UT at all stations. These enhancements are present over a large height interval, from 200 km to 450 km. It is also worth noting that the stations at lower latitudes observe stronger enhancements. This is in agreement with the suggestion by Jones and Rishbeth [1971] that the intensity of the positive ionospheric storm effect is proportional to $\cot I / NmF2$, where I is a magnetic dip angle. Thus, for the Chilton and Athens the ratio between the expected intensities is ~ 0.7 to 0.8 . Another difference between the quiet and disturbed days is the absence of the post-sunset enhancement of the electron density (approximately between 18 UT and 20 UT) on the storm day. Thus, on this day, both positive and negative effects are observed sequentially in the European sector. It is also noticeable that

the height of the maximum electron density moves upward on the disturbed day with respect to the quiet day values. To investigate the height changes more quantitatively we make use of the foF2 and hmF2 characteristics deduced from the electron density profiles. Figure 28 illustrates the comparison of the layer characteristics recorded on 24 August 2005 to the quiet day values. For better orientation, the DST index variation is plotted in the top panel showing storm commencement and the following main and recovery phases.

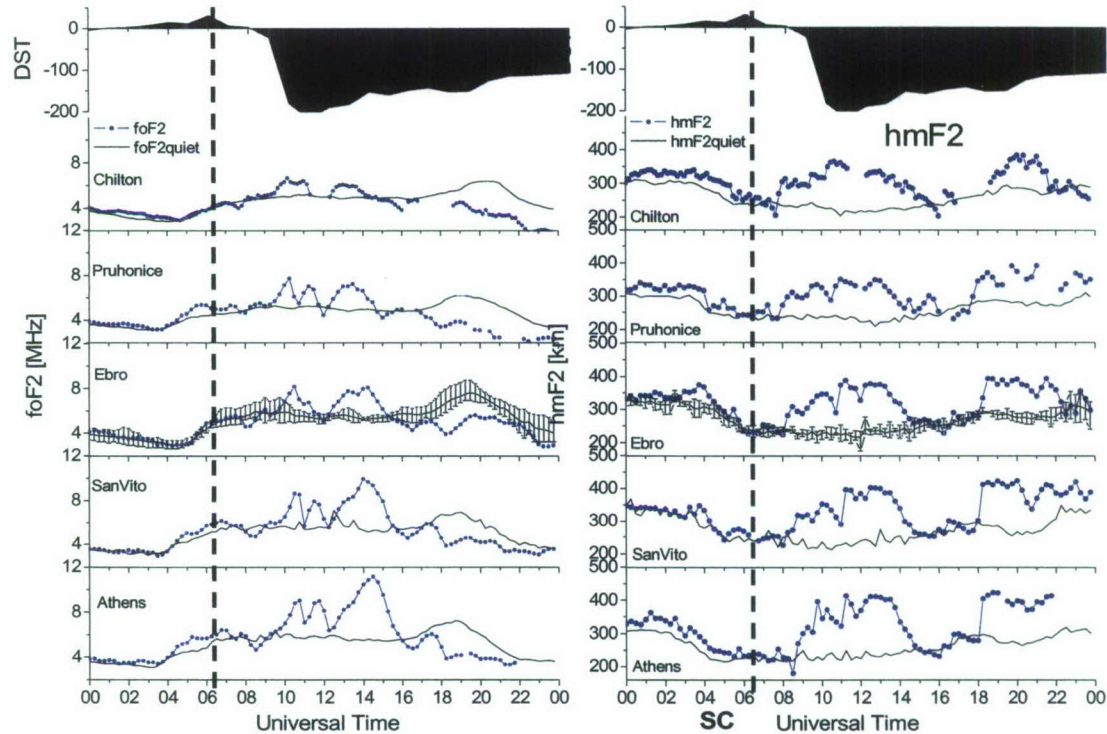


Figure 28. Variation of foF2 and hmF2 layer parameters on 24 August 2005 compared to the quiet day averages (black curves). Top panel shows DST index.

The data presented here show a clear deviation of the foF2 and hmF2 values observed on the event day compared with the quiet day pattern emphasizing both positive and negative (after 16 UT) effects at all stations. The Ebro station plot shows the range of foF2 and hmF2 values for the four quiet days used in calculating the average. The uplifting observed on the disturbed day is significantly larger than the height variations on quiet days. There are two major periods of strong ionospheric uplifting in these data: the first one lasts from 08 UT to 14 UT and the second one lasts from 17 UT to 22 UT. They roughly correspond to the positive and negative phases of the storm. Before looking at the effect of ionospheric uplifting and its relation to the electron density enhancement/depletion in greater details, the observations made in the American sector are shown in Figure 29 to be compared to the European sector. Figure 29 is in the same format as Figure 28 and shows the foF2 and hmF2 parameter variations on the disturbed day and the average quiet values. The American station coordinates can also be found in Table 5. It is worth noting that in the American sector the storm commencement at 0613 UT and the following main phase both occur during local nighttime.

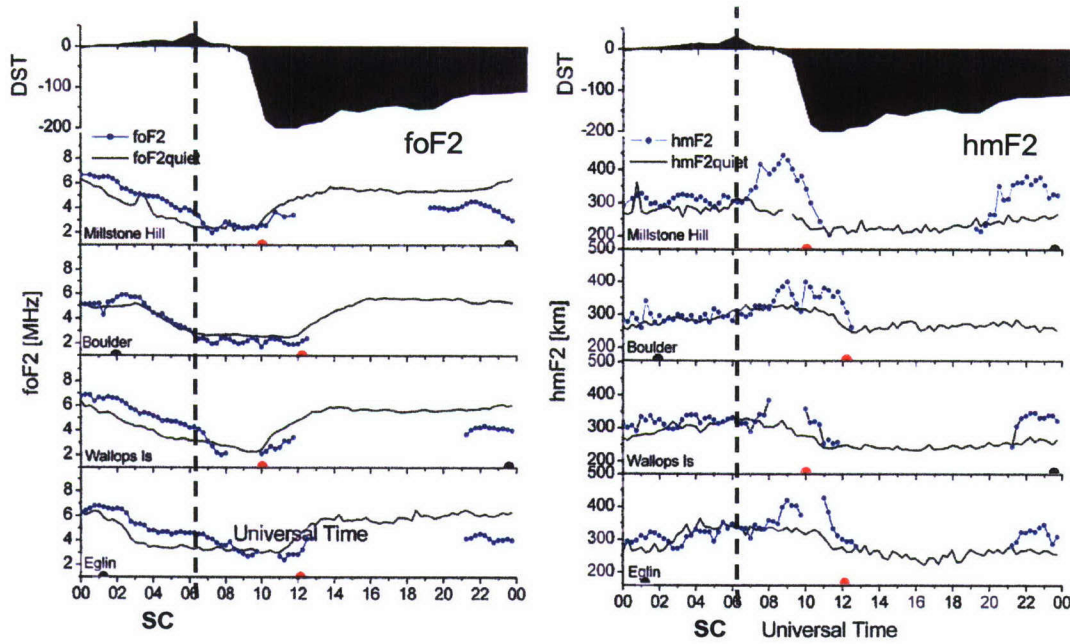


Figure 29. American sector data for 24 August 2005 storm. Plots show variations of foF2 (left) and hmF2 (right) as compared to the quiet day averages (black curves).

In Figure 29, there appear to be times when foF2 and hmF2 cannot be measured. It is known that ionospheric storms affect higher altitude regions of the ionosphere severely [e.g., Buresova, 2005]. Thus, during a negative storm the foF2 parameter can experience dramatic reductions, while foF1 is only slightly changed. This often leads to a situation in which $\text{foF2} \leq \text{foF1}$, and for an ionosonde this means that the F2 layer is “shadowed” by the F1 layer. Under such circumstances, measurements of both foF2 and hmF2 are impossible (this is referred to as a “G-condition” in the ionogram processing handbooks), however, the upper limit of foF2 can be estimated as equal to foF1. The G-condition is often observed in summer daytime at mid-latitudes when the F1 layer is well developed. Such conditions were observed on 24 August 2005 in the American sector stations after sunset.

The behavior of the ionosphere in the American sector on the storm day is distinctively different from that in the European one. In comparison to the quiet day pattern, we see an overall decrease in the electron density, *i.e.*, a negative ionospheric storm was observed at the US stations. In Figure 29, one can also see that following the storm commencement the stations observe an uplifting of the ionosphere, similar to the one detected by the European stations. We now need to investigate this uplifting effect in both sectors in more detail by using the hmF2 parameter as a measure of the ionospheric height variations. Figure 30 presents the differences between the hmF2 values measured on the event day and the quiet day averages for both the American and European sectors. These differences are plotted as a function of time elapsed from the storm commencement at 0613 UT.

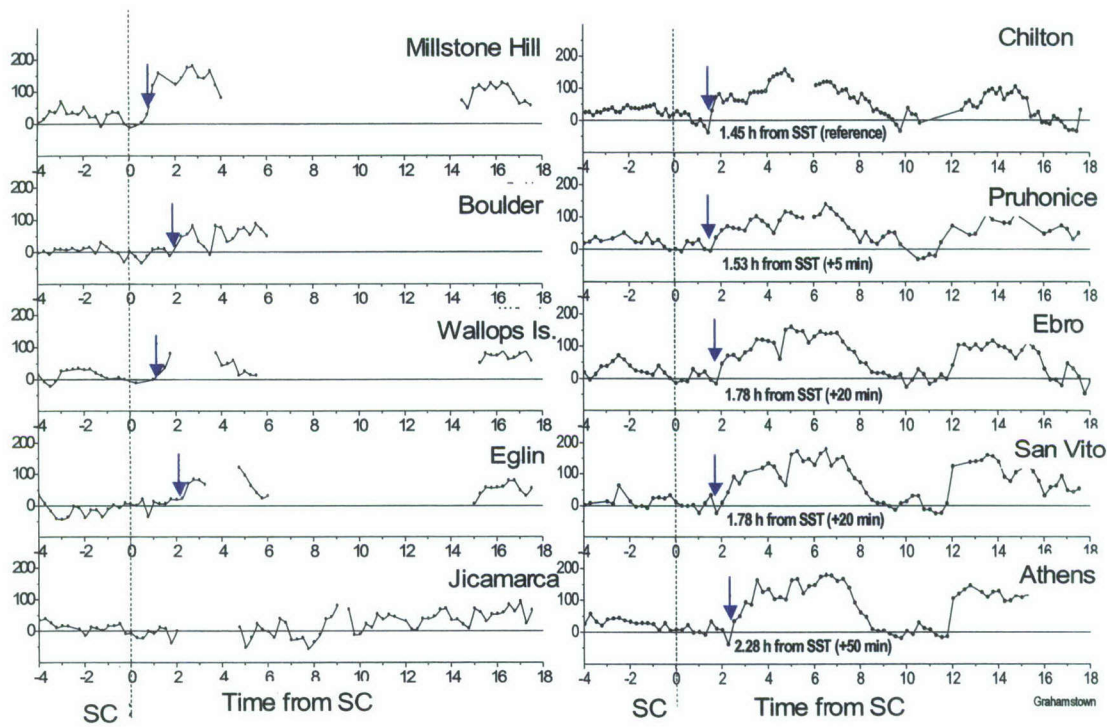


Figure 30. Difference between hmF2 values measured on the event day and the quiet day average as a function of time after storm commencement.

The approximate beginning of the F layer uplifting is indicated by arrows. It is clear that in the European sector, the delay between the storm commencement and start of the uplifting is measureably larger than that in the American sector. The minimal delay is 105 minutes in the European sector (Chilton) and less than 60 minutes in the American sector (Millstone Hill). Moreover, it is clear (at least for the European sector data) that the delay increases as one moves from higher to lower latitudes. This suggests that the disturbance associated with the ionospheric storm is propagating from high to low latitude. Another interesting observation comes from the American sector data. Here one can see that the Millstone Hill and Wallops Island have a time offset of one hour or less, while the Boulder and Egin observe an uplifting at least 2 hours after the storm commencement. Apparently, longitudinal separation plays a significant role in the uplift onset time. In other words, the initial neutral wind surge on the night side appears to be limited on the west side to a boundary near 01 LT (position of the Millstone Hill station at 0613 UT). Note that for this negative storm in the American sector, the uplifting by itself does not correlate with the density depletion as it takes another 2 to 3 hours for the US stations to observe the foF2 decrease. This total time delay obviously consists of the composition bulge's equatorward progression and also of the ionospheric plasma response to the increased recombination rate. In the next section we try to put these results of these observations together as a coherent model.

7.3 Discussion

Our observations of the 24 August 2005 storm are consistent with the idea that the major driver of storm effects at mid-latitudes is the neutral wind. A simplified picture of the ionospheric response to the storm is as follows [Prölss, 1993; Fuller-Rowell et al., 1994]. A strong energy input in the auroral zone during the initial phase of the storm results in an increase of the Joule heating that drives a global neutral wind surge. Divergence of the horizontal winds leads to vertical winds causing a composition change in the upper atmosphere, namely, a change in the O/N₂ ratio. This increase in O, in turn, leads to a higher recombination rate, which reduces overall electron density in the ionosphere. Thus, in the region of the composition change, a negative ionospheric storm is expected. Such a region of increased O/N₂ ratio is often referred to as a “composition bulge”. This composition bulge is usually created on the nightside in the region of 0 to 4 LT and then rotates with the Earth and is also pushed by background neutral winds. The dayside ionosphere typically observes positive storm effects as the horizontal meridional wind surges originating in the auroral oval push the ionosphere upward along the magnetic field lines [Rishbeth, 1998] to the region of lower recombination rate thus leading to electron density enhancement after the start of the storm. It is important to note that during the positive phase the increase in the ionization density lags the increase of layer height by 1 to 2 hours. This is how long it takes to build up an increased ionospheric plasma density in response to the uplifting of the F layer. The ionospheric response observed in our analysis of the digisonde data is in good agreement with this explanation of storm dynamics. We have illustrated this with the 24 August 2005 storm for which these data were presented in detail. First, let us take a look at the energy input in the auroral region. Figure 31 presents a composite observation plot made at 0652 UT (storm commencement was 0613 UT), showing net energy flux. This plot is made using the OVATION database (<http://sd-www.jhuapl.edu/Aurora/ovation/index.html>). We see that the oval was significantly expanded, particularly on the nightside its equatorward edge practically reached the Millstone Hill station. In the American sector, all the digisonde stations observed a negative storm effect relatively quickly after the storm commencement in agreement with the oval observations. Given the distance from the northernmost station to the oval, it is natural that there is a small time delay between the storm onset and the observed response at the Millstone Hill. This negative effect is obviously caused by the composition bulge surging in from the auroral oval. At the Millstone Hill station, we also observed a strong uplifting of the ionospheric electron density maximum, which is evidence of the presence of horizontal neutral wind (that moves the ionosphere upward along the magnetic field line). At other American stations, the uplifting effect is not so clearly detected because of the presence of the G-condition that made it impossible to measure the height of the layer peak.

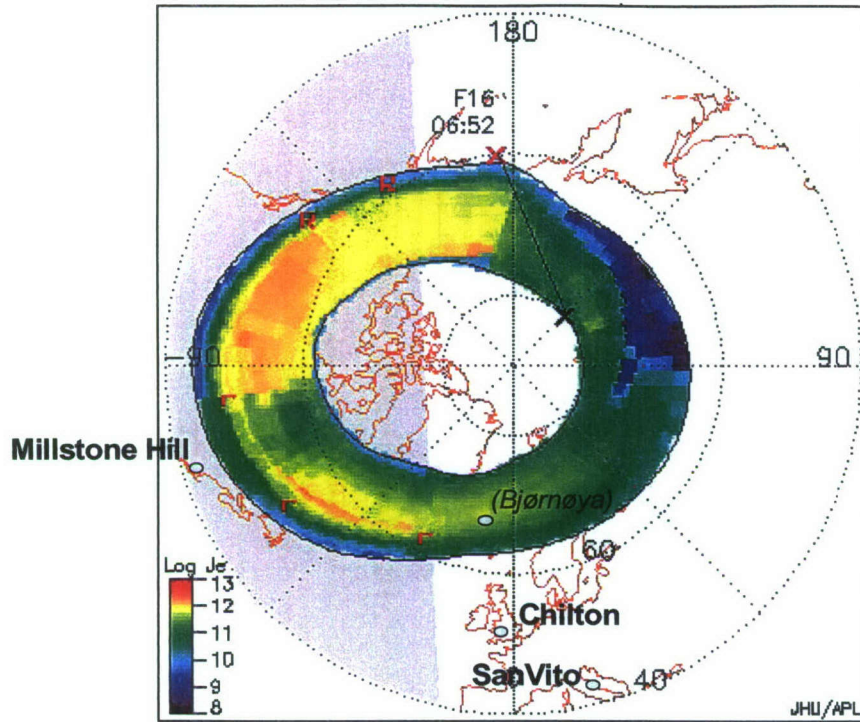


Figure 31. The 24 August 2005 storm. Color scale shows the energy input determined from radar and DMSP satellite measurement. These data are taken from OVATION database. The locations of selected digisonde stations as well as Bjørnøya magnetic observatory are shown in the plot.

Figure 32 presents composite plots showing the superimposed variations of Δf_oF2 and Δh_mF2 parameters measured in the European sector. We see that at all stations the increase in the Δf_oF2 parameter occurred 1 to 2 hours after the beginning of the increase in Δh_mF2 parameter as is expected for the positive storm effect caused by the neutral wind disturbances. It is interesting that this time offset is noticeably shorter at the lower latitudes stations compare to those at the higher latitudes (1 hour at Athens versus 1.5 hour at Chilton). This interesting result needs additional research to be better understood. Our measurements at spatially separated points also make it possible to determine the equatorward propagation speed of these disturbances. If measured by the leading edge, *i.e.*, by the beginning of the increase in the Δh_mF2 parameter, then the TAD propagation speed is between 400 m/s and 900 m/s, which is within the range of the expected TAD velocities (for instance, Hocke and Schlegel [1996] report an average speed for the waves originating in the auroral latitudes of 200-1000 m/s). Given the time offset of 1.45 hour between the storm commencement time and the height increase at the Chilton station (see Figure 30) this TAD propagation velocity puts the source of the disturbance causing the positive effect in the European sector about 3000 km north of the Chilton station. This corresponds to the vicinity of the Bjørnøya station in the middle of the auroral oval shown in Figure 31 and is in agreement with the neutral wind-based storm model.

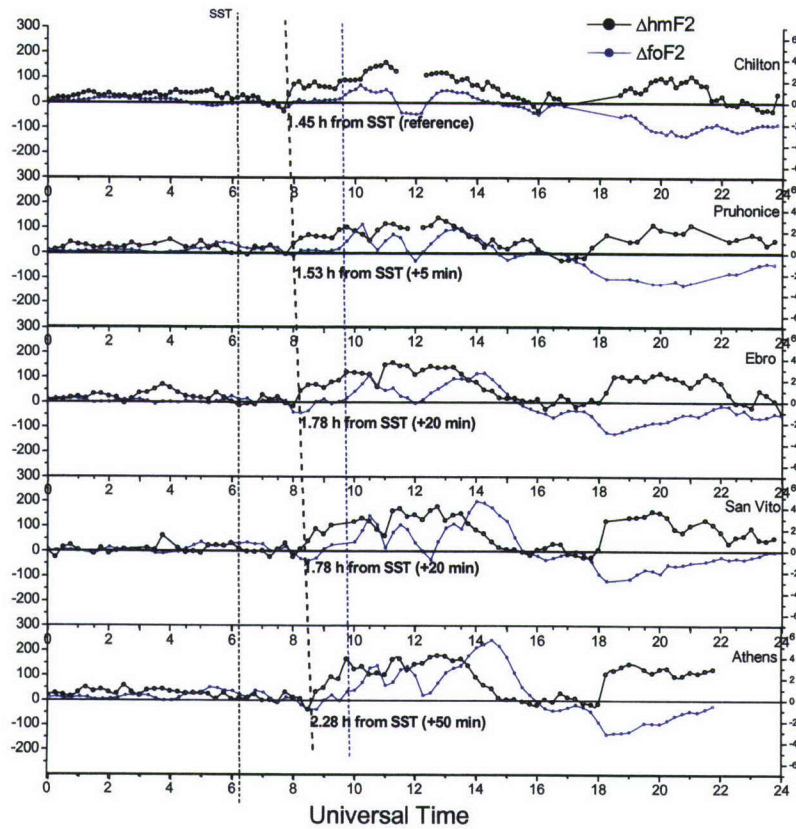


Figure 32. Variations of the $\Delta hmF2$ (black) and $\Delta foF2$ (blue) parameters measured in the European sector. The increase in the electron density lags height increases at all stations. A vertical line indicates the storm commencement time (SST). The sloping lines connect the starts of the increases in $hmF2$ (black line) and $foF2$ (blue line).

After 18 UT, the European stations (positioned in the local time sector 18 to 20 LT) observe the negative phase of the storm. Fuller-Rowell et al. [1994] have shown in their simulation that 12 hours into the storm time, composition disturbance can occupy a very large area, essentially covering the whole nightside ionosphere at mid-latitudes. Therefore, it is not surprising that so long after the beginning of the storm, the European stations have “drifted” into the zone of the disturbed composition and thus began observing a negative effect. The fact that the easternmost station, Pruhonice, appears to have detected the negative phase first is supporting such a scenario.

7.4 Summary

We have found the data from the global digisonde network very useful in our study of ionospheric storm effects. For this report, we mainly concentrated on the 24 August 2005 storm. Digisonde $foF2$ and $hmF2$ data from the stations in the American and European regions provided experimental evidence supporting the storm model based on the leading role of the neutral wind

and the thermospheric circulation. The major results testifying to the validity of this mechanism are the observation of the ionospheric uplifting preceding both negative and positive electron density storm phases. Unlike other experimental works done previously, in these sounder observations we directly measure the height of the ionosphere by inverting the vertical sounding data. Simultaneous observations at a number of the stations is also a key part of our experiment. The latitudinal chain of ionosondes in the European sector observed the propagation of the disturbance and estimated its speed which places it into a class of the gravity waves/traveling atmospheric disturbances. Data presented here suggest that the composition disturbance zone responsible for the negative storms has a tendency to form around the sector of 03 to 05 LT. On the other hand, positive storms prefer to begin at around local noontime. Recently, there also has been a lot of attention paid to the effects of the prompt penetration of the electric field (*e.g.*, Foster and Rich, 1998; Huang et al., 2005). It has been shown that penetrating electric fields are also capable of producing ionospheric storm effects. A characteristic feature of this mechanism is a near-simultaneous effect at a large range of latitudes. The effects of the penetration electric field are also typically short lived, usually less than half an hour (some longer lasting effects have been reported lately as well [Huang et al., 2005]). The observations we presented cannot rule out the penetration field mechanism, but the data collected does strongly support the neutral wind scenario for the ionospheric storm.

8. ROUTINE HF ABSORPTION MEASUREMENTS USING DIGISONDES

8.1 Approach

To determine the diurnal variation of radiowave absorption using the echo amplitudes measured with an ionosonde, it is necessary to determine the radiated power of the specific sounding system used for these measurements. The effective system gain is defined as the product $P_T G_T G_R$, where P_T is the transmitted power in Watts, G_T and G_R are the transmitting and receiving antenna gains, respectively. The received power is, in terms of these factors, given by the Friis formula:

$$P_R(f) = \frac{P_T G_T G_R(f) \lambda^2}{(4\pi)^2 h^2} \frac{1}{L(f)} (W)$$

where λ is the free space wavelength, h is the path length (2 x the reflection height), and L is the combined losses which include D-region absorption in the daytime and F-layer reflection losses. As discussed in detail in the next section, the calibration of the ionosonde system uses the midnight time period data when there is no D-layer present. Assuming, temporarily, that the combined losses $L=0$ during the selected nighttime hours, the system's effective gain at a given frequency is:

$$P_T G_T G_R = \frac{(4\pi)^2 h^2}{\lambda^2} P_R$$

where P_R is the received power derived from the measured receiver output voltage. Soundings are made every 15 minutes during this period with a frequency step of 50 kHz. The frequency

range for the calibration presented here is limited by the F-layer critical frequency during the nighttime period. Here the frequencies selected for this analysis are 2.5 through 5.3 MHz in steps of 0.4 MHz. In order to increase the number of data points at each frequency, nearby frequencies are combined, e.g., at 2.5 MHz, five frequencies 2.40, 2.45, 2.50, 2.55 and 2.60 MHz were used to obtain an averaged output amplitude. For calibrating the sounder system over the largest possible frequency range, the data for the months of May through August 2005 were used. These “summer” months had the highest F-layer critical frequencies during the nighttime calibration period.

8.2 System Calibration

To calibrate the sounder ionogram amplitude data, the hours from 05 through 09 UT (22 – 02 LT) were combined (as well as the closely spaced frequencies discussed above) when it was reasonable to assume that the nighttime ionosphere was relatively stable during these four hours on each of the nights. In addition, it was assumed that there was no D-region absorption during these late hours. The Digisonde 256 located in Boulder, CO, was selected for this analysis. This sounder was chosen for this preliminary investigation because it was well maintained during this analysis period. For the four months discussed above, the number of potential nighttime amplitude measurements exceeded 8000 per frequency. In fact, for a variety of reasons, the actual number of samples used to determine the average $P_T G_T G_R$ varied from 6500 for 2.9 MHz down to 2100 for 4.1 MHz (see Figure 33).

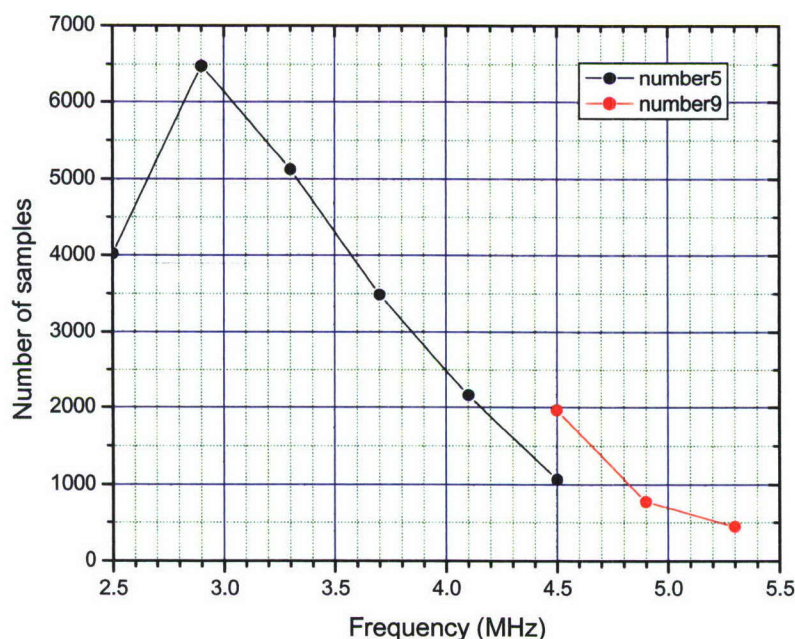


Figure 33. Number of amplitude measurements used to determine the average $P_T G_T G_R$ as a function of sounding frequency.

For frequencies above 4.1 MHz, the number of samples over the four months became progressively smaller and it was decided at these higher frequencies to average nine adjacent frequencies rather than the five used for the lower frequencies. These small sample sizes were caused by the relatively infrequent occurrence of the higher F-layer critical frequencies. The short curve in Figure 33 shows the number of samples used at 4.5 MHz and above.

Figure 34 shows the spread in the nighttime values of $P_T G_T G_R$ for 2.9 MHz. These data show an extreme range of greater than 40 dB. However, 93 percent of the measurements lie between 180 and 196 dB, while 62 percent of the points lie between 186 and 192 dB; a range of only 6 dB. Similar distributions were calculated for each of the other seven frequencies used in this analysis.

The factors that contribute to this spreading are, first, focusing and defocusing of the reflected signal caused by irregular structure in the ionosphere, and second, the variation in the reflection coefficient of the F-layer in different nights. These two issues are addressed in the next section.

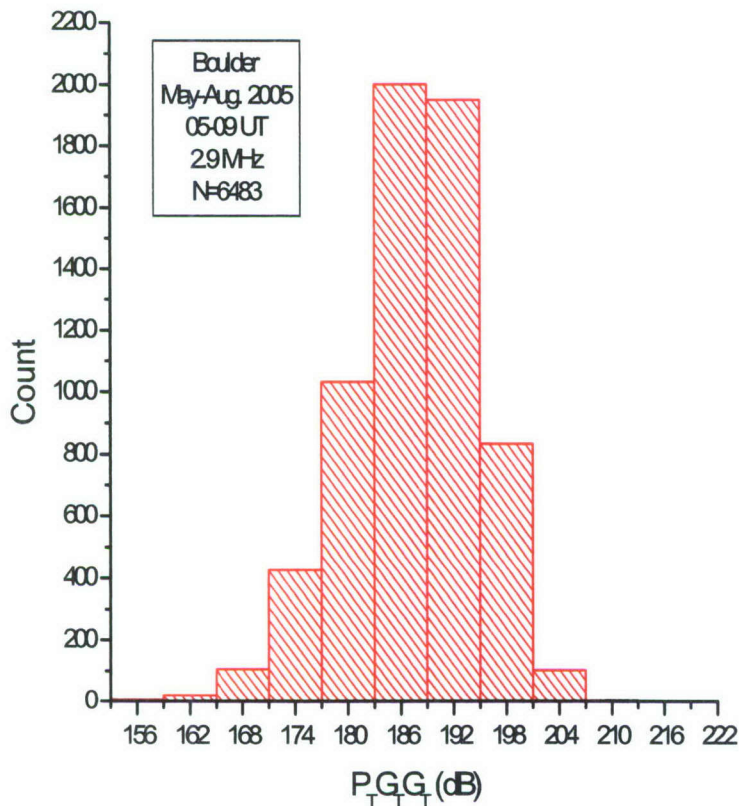


Figure 34. Histogram of the digisonde derived $P_T G_T G_R$ values over the nighttime period from May through August 1005 for 2.9 MHz.

A similar analysis was used to determine $P_T G_T G_R$ for each frequency.

9. FOCUSING AND REFLECTION CALCULATIONS

Addressing the issues in the use of the Friis equation above, it was recognized that there were two factors not accounted for in the nighttime calibration calculation. The first of these was the focusing/defocusing of the reflected energy by ionospheric irregularities and the second, the losses at the reflection from the nighttime F-layer. These are addressed in the following sections.

9.1 Focusing Gain

To better understand the effects of ionospheric irregularities on the focusing and defocusing of the reflected radio energy, a program was written that generates a random reflecting surface with a specific average horizontal structure length and an RMS amplitude. Figure 35 shows a schematic of the reflection process from this irregular surface and illustrates focusing gain. Focusing gain was defined here as the ratio of the number of rays reflected from the irregular surface that fall within a circular area within a Fresnel radius ($r_F = \sqrt{2h\lambda}$ where h is the reflection height and λ is the free space wavelength) to the number of rays in the same area when the reflecting layer was smooth. For the sounding frequencies used in this study, the Fresnel radius was of the order of 10 km. For these simulations, sounding frequency is not an important factor as it enters only in the Fresnel radius as a square root and the focusing gain ratio tends to diminish the effect of that factor as well. The focusing simulation program was automatically repeated 100 times to develop a reliable statistical description of the focusing/defocusing gain.

Figure 36 shows the results of the calculation of the focusing gain's 100 independent trial runs (negative gain is defocusing). For these calculations, the gain was binned in 3 dB steps. For the most shallow amplitude run (RMS amplitude = 0.1 km), the result was close to what would have been expected from a smooth reflection surface, *i.e.*, all the samples fall in the 0-dB gain bin. As the reflecting screen depth was increased to a maximum of 5 km, the spread in focusing gain tends to increase to a maximum of 6 dB.

The same program was then run (100 realizations each) for four horizontal scale sizes: 4.3, 8.4, 17.0, and 33.0 km and each of these with four amplitudes: 5, 10, 15, and 20 km. These calculations are summarized in Figures 37a-37d showing the percentage of 100 realizations with positive focusing gain (>1.5 dB), zero gain (between -1.5 and +1.5 dB) and negative gain (<-1.5 dB).

The trend associated with these calculations is clear. For each vertical amplitude selected here, there is a horizontal structure size that yields the greatest focusing gain. The maximum gain in these calculations moves to larger horizontal structure sizes as the RMS amplitude increases, always reaching 80% or more positive focusing gain. The median focusing gain maximum for each vertical amplitude case is shown in the Table 6.

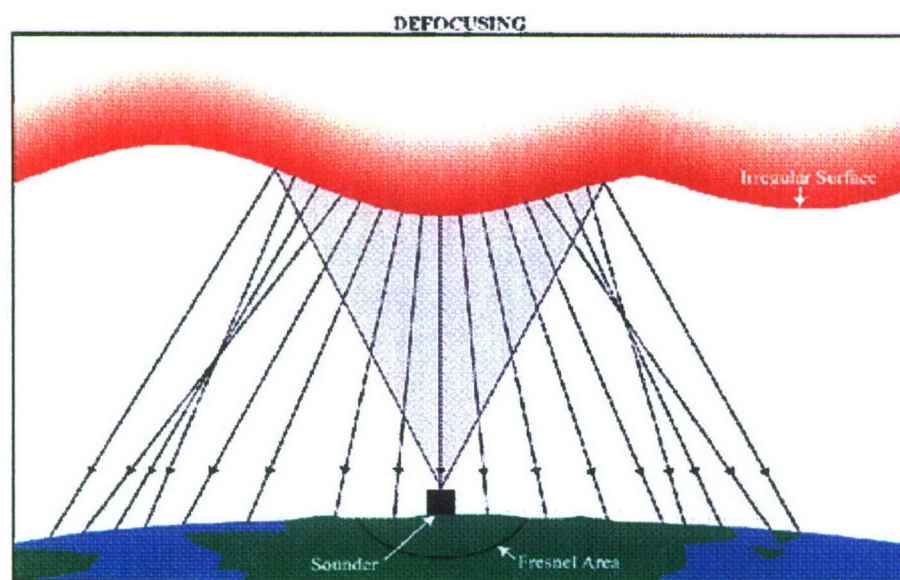
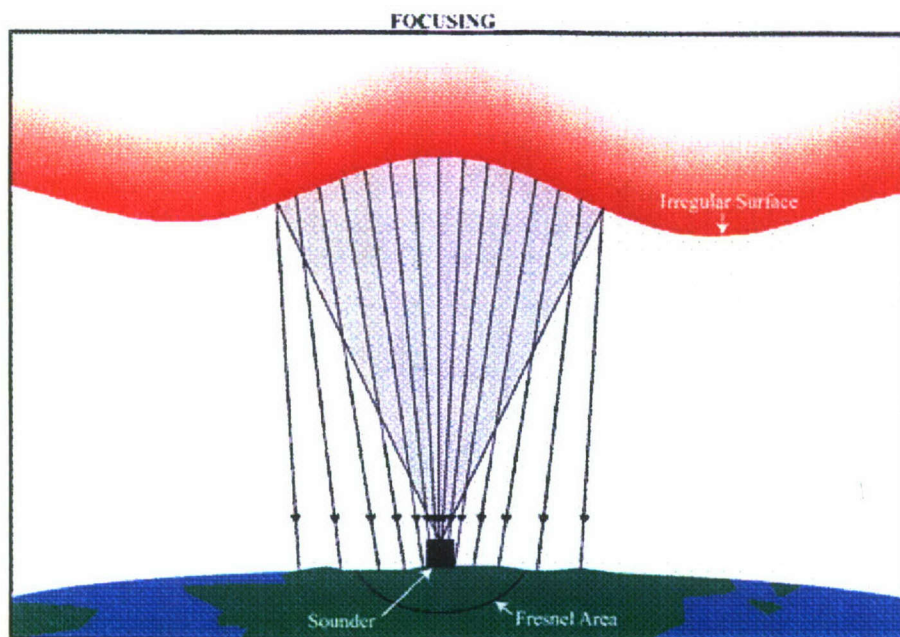


Figure 35. Illustration of focusing and defocusing gain associated with an irregular reflecting surface.

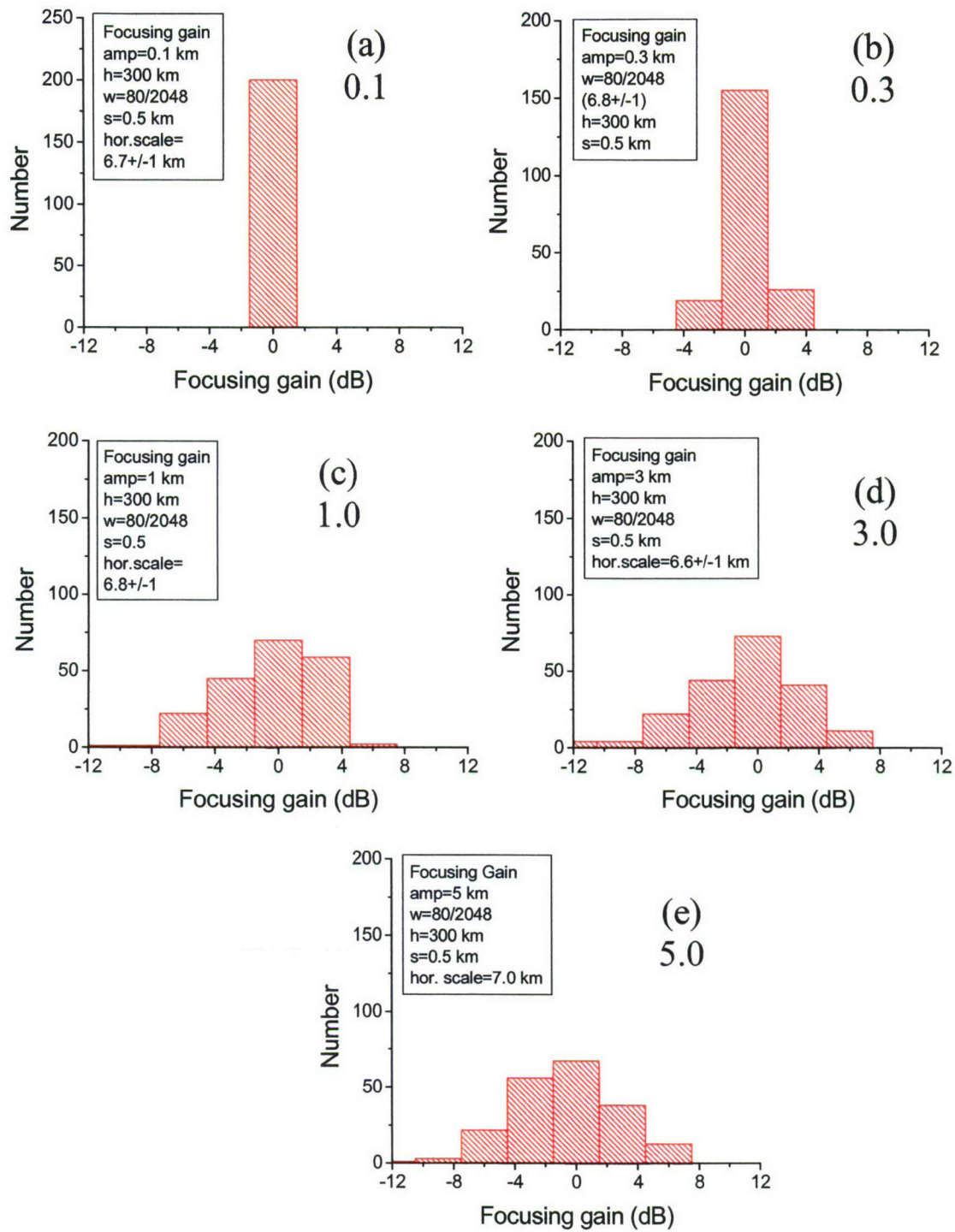


Figure 36 Distribution of 100 realizations of an irregular reflecting surface with RMS amplitudes varying from 0.1 through 5.0 km. In all cases the horizontal scale size was ≈ 6.8 km.

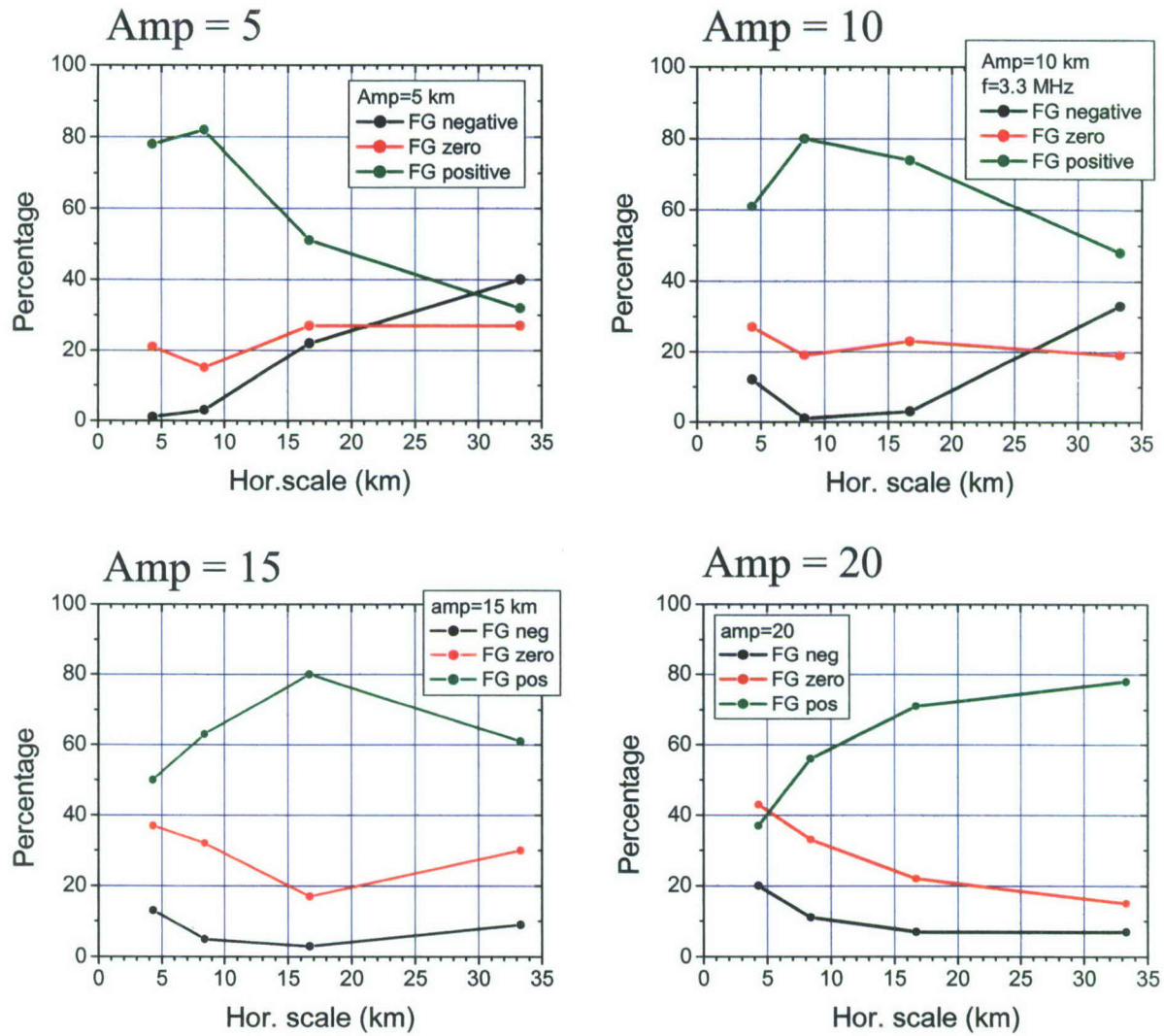


Figure 37. Percentage positive and negative focusing gain as a function of horizontal structure size for several vertical RMS amplitudes: a) 5 km, b) 10 km, c) 15 km and d) 20 km.

Table 6. Maximum Focusing Gain and Associated Irregularity Horizontal Structure Size as a Function of RMS Amplitude

RMS amplitude (km)	Hor. structure size for maximum gain (km)	Max. focusing gain (dB)
5	8.4	3.1
10	12.0	2.8
15	17.0	2.8
20	33.0	3.1

These maximum focusing gains appear to hold over a wide range of structure sizes for all the selected amplitudes and a good estimate of overall focusing gain was 3 dB.

9.2 Nighttime F-Layer Reflectivity

The second issue addressed here is the assumption made earlier that the nighttime losses were zero. The issue of reflection from a layer with a gradient in the electron density is examined. The question to be answered is how does the reflection coefficient depend on the local electron density gradient at the reflection altitude when there are no absorbing layers below the reflection level?

This issue was raised when the variation of the nighttime losses was examined on five sequential nights (3 May-7 May 2005). Figure 38 shows the variation of the losses on each individual night and they appear to be relatively constant. However, the average nighttime loss varied by more than 10 dB over these five nights. This is well illustrated in Figure 39 which shows the mean loss on each of the five nights with bars that indicate the spread in the individual nighttime values.

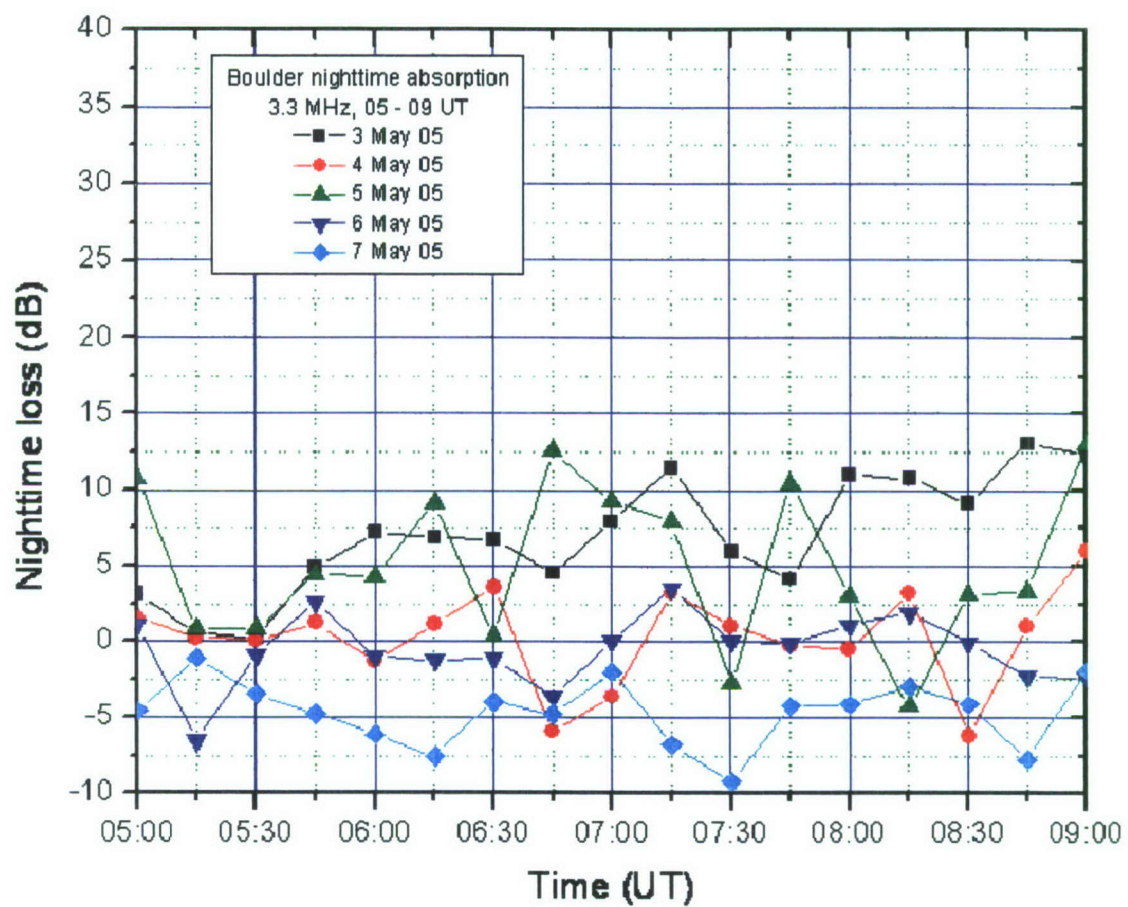


Figure 38. Boulder measured nighttime loss (05-09 UT) on five sequential days.

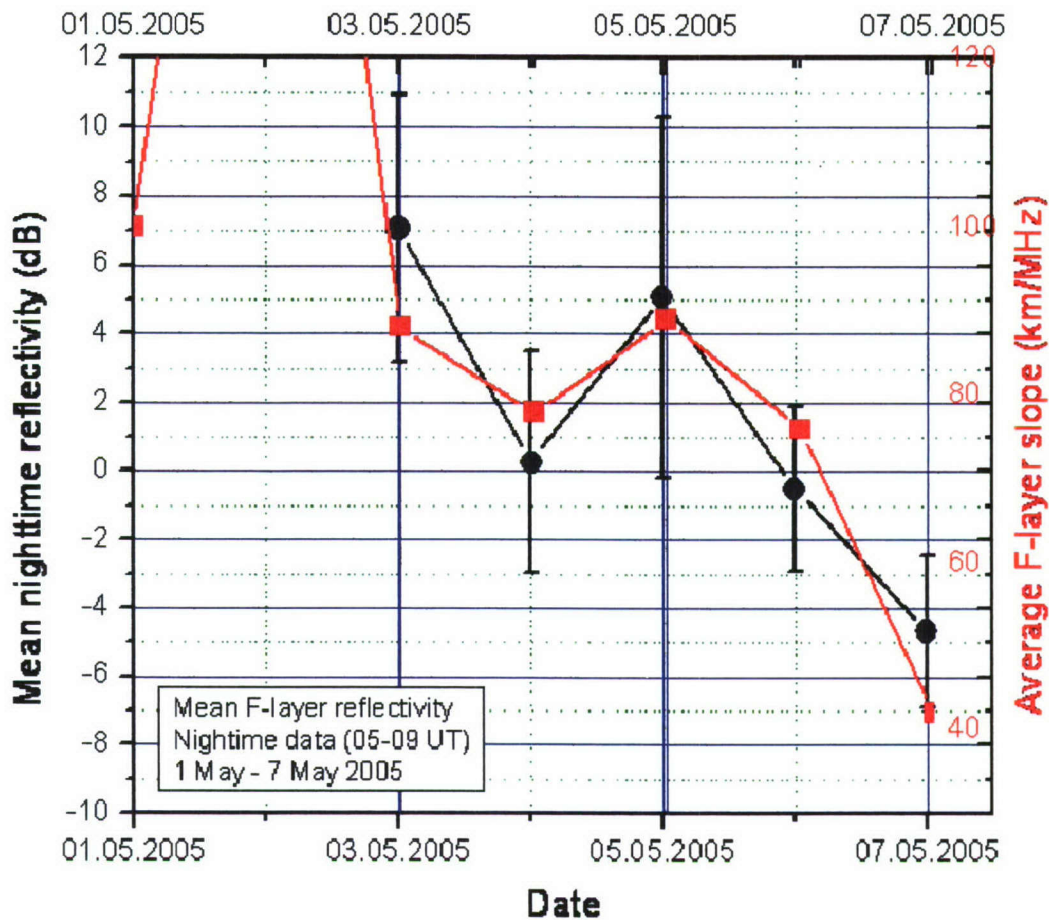


Figure 39. Mean loss over the hours from 05-09 UT on sequential nights from 3 May – 7 May 2005 (dots). Calculated mean F-layer slope (km/MHz) using the ionograms for the period from 1 May-7 May 2005 (squares).

Superimposed on the data curve is the mean F-layer slope defined here as the ratio of the height difference between the layer peak and bottom divided by the measured foF. Although the scales for these two curves are very different, the similarity of the general shape of the curves indicates a good correlation between reflection loss and layer slope. To better support this conjecture, a review of the theory of the amplitude of the reflected waves is examined in the next section.

9.3 Reflectivity Theory

At this time, only a preliminary examination of this issue is possible. The early works of Rawer [1939], Rawer and Suchy [1967], and Budden [1988] have investigated the layer reflection coefficient by finding solutions to the wave equation in a plasma for the up going and down going waves. Using a symmetrical Epstein electron density profile, they calculated the

reflection coefficient as a function of sounding frequency (normalized by the peak plasma frequency of the layer) for several layer thicknesses (see Figure 40).

$$\nu = 0.02 \omega_p (\text{max}) \quad (\beta - \text{curve})$$

$$\nu = 0.10 \omega_p (\text{max}) \quad (\gamma - \text{curve})$$

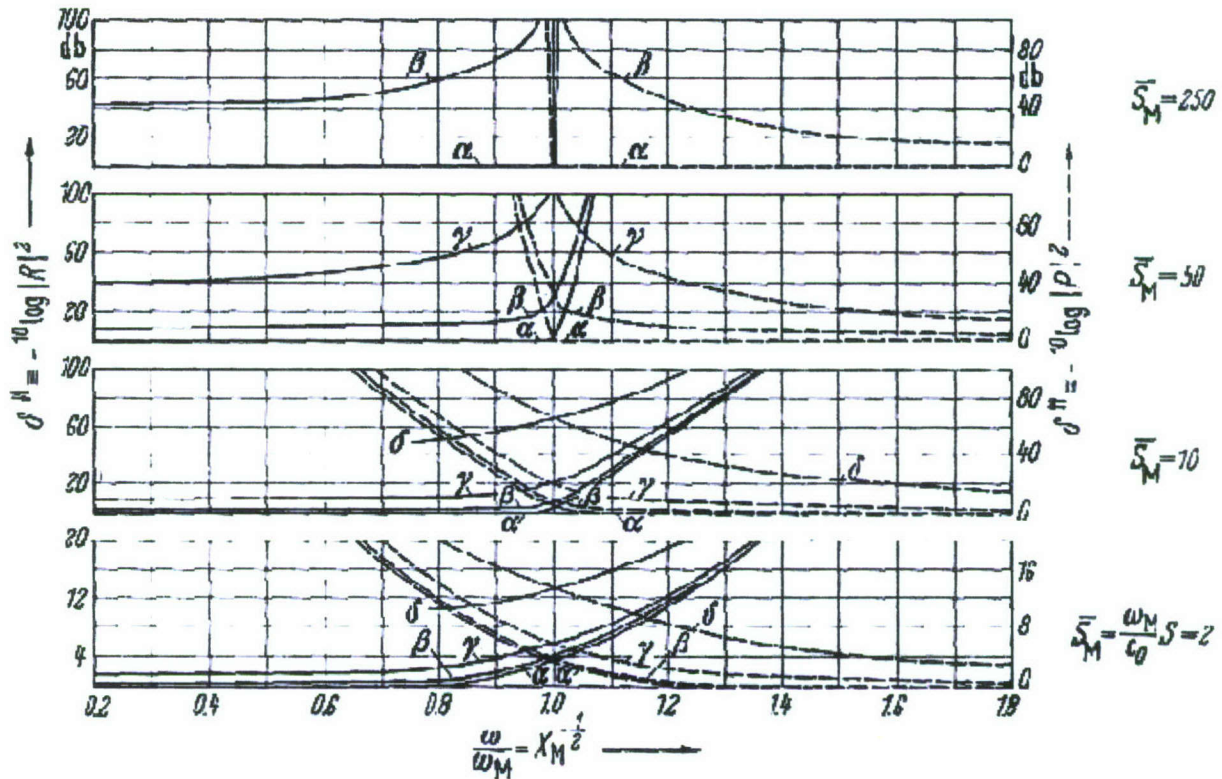


Figure 40. Reflection index ($20 \log |R|^2$) as a function of sounding frequency for normalized layer thicknesses varying from 2 (thinnest) to 250 (thickest) in three factors of 5. (Rawer and Suchy, p. 194, Figure 64).

Here, collision frequencies were expressed in terms of its ratio to the maximum layer plasma frequency. The two curves in Figure 40 (marked β and γ) were compared to the collision free case (α -curve). Figure 41 shows this reflection coefficient as scaled from the above curves for

$$f = \frac{f_{p, \text{max}}}{2}.$$

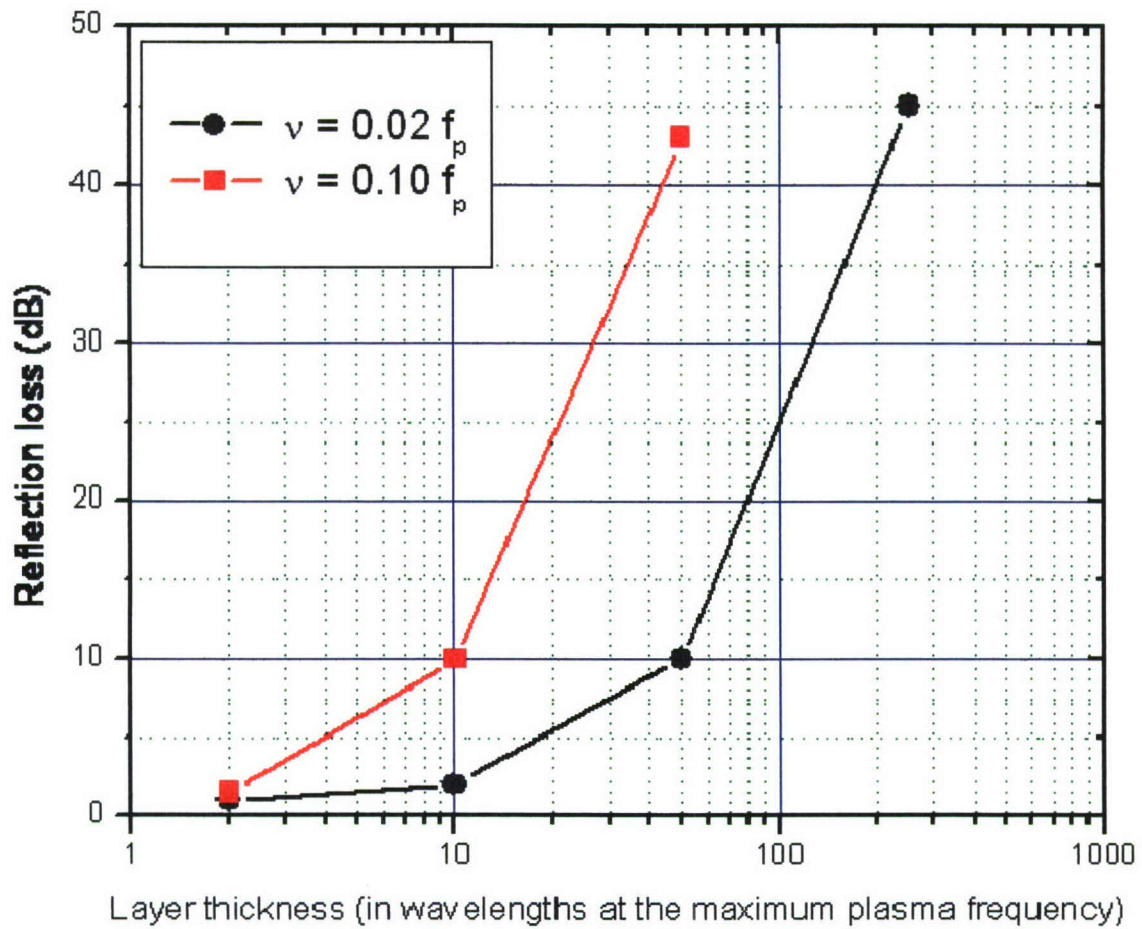


Figure 41. Reflection loss (dB) as a function of normalized layer thickness for two collision frequencies.

These results are considered preliminary (again the reflection losses increase rapidly with increasing layer thickness which implies a smaller electron density gradient) so more effort is required to definitively characterize the nature of the reflection process from the F-layer with a realistic gradient.

10. CALIBRATION / VALIDATION OF DMSP UV MEASUREMENTS OF THE F2 PEAK CHARACTERISTICS WITH DIGISONDE MEASUREMENTS

The DMSP (Defense Meteorological Satellite Program) F17 weather satellite was launched on November 4, 2006. It has two optical instruments onboard:

SSULI - limb scanning ultraviolet imager / spectrometer (built by the Naval Research Laboratory)

SSUSI - nadir scanning ultraviolet imager /spectrometer and photometer (built by the Applied Physics Laboratory, Johns Hopkins University). The satellite has an almost polar orbit with a period of 101.9 min, an apogee of 856 km, a perigee of 841 km and an inclination of 98.8°.

The digisonde ground-based electron density profiles served as “ground truth” for the satellite-borne UV optical measurements of F layer electron densities. Aerospace Corporation was responsible for identification of “fly-over” events such that the satellite and digisonde measure the same region of the ionosphere at about the same time. The satellite data includes both surface and limb-scan measurements. The fly-over calculation results in at least one event per 24-hour period for each participating digisonde. Each event represents a one-hour interval for which UMLCAR provided manually scaled ionogram data in SAO 4.3 format with 15 minutes cadence (can be different for non-DISS network sounders). In total, 36 stations were considered as candidates for Cal/Val project, however, stations located in the vicinity of the South Atlantic Anomaly (SAA) were excluded (6 stations). The following is the list of approved stations.

Station Name	Geo. latitude	Geo. longitude	Mag. latitude
Jicamarca	-12	283.2	-1.78
Kwajelain	9	167	3.6
Fortaleza	-3.8	322	4.73
Sao Luis	-2.6	315	6.41
Hainan Island	19.4	109	9.14
Chung-Li	25	121.2	14.99
Madimbo	-22.38	30.88	-19.79
Wuhan	30.6	114.4	20.4
Osan	37.1	127	27.33
Ramey	18.5	292.9	28.72
Boulder	40	254.7	-31.25
Learmonth	-21.3	114	-31.99
Athens	38	23.6	36.35

San Vito	40.6	17.8	39.89
Eglin	30.4	273.2	40.26
El Arerosillo	37.1	353.333	40.8
Point Arguello	34.7	239.4	41.04
Dyess	32.5	260.3	41.41
Rome	41.9	12.5	42.09
Irkutsk	52.4	104	42.17
Roquetes/Tortosa	40.8	0.3	43.19
Bundoora	-37.72	145.05	-45.62
Pruhonice	50	14.6	49.55
Dourbes	50.1	4.6	51.43
Millstone Hill	42.6	288.5	52.86
Chilton	51.5	359	53.76
Wallops	37.9	284.5	54.04
Fairford	51.7	358.5	54.04
Juliusruh	54.6	13.4	54.17
Goose Bay	53.3	300	63.27

Requests for following stations have been processed.

Station Name	Geo. latitude	Geo. longitude	Mag. latitude
Jicamarca	-12	283.2	-1.78
Kwajelain	9	167	3.6
Fortaleza	-3.8	322	4.73
Sao Luis	-2.6	315	6.41
Madimbo	-22.38	30.88	-19.79
Ramey	18.5	292.9	28.72

Table 7 shows the status of the data requests for the period of January 1, 2007, until September 30, 2007.

Table 7. CalVal Digisonde Data Request Status

Request status	Number since January 1, 2007
Total requests	138
Requests loaded to DIDBase	122
Requests not loaded (ADRES system is waiting for data availability)	16
Not available (no data) requests	14
Loaded but not scaled requests	0
Scaled and reported requests	122
Scaled and reported ionograms	533

11. PUBLICATIONS

The following list of journal publications have all acknowledged support under AFRL Contract No. FA8718-06-C-0072.

Chen, W. S., C. C. Lee, J. Y. Liu, F. D. Chu, and B. W. Reinisch, Digisonde spread F and GPS phase fluctuations in the equatorial ionosphere during solar maximum, *J. Geophys. Res.*, *111*(A12), A12305, 10.1029/2006JA011688, 2006.

Galushko, V. G., A. S. Kascheev, V. V. Paznukhov, Yu M. Yampolski, and B. W. Reinisch, Frequency-and-angular sounding of traveling ionospheric disturbances in the model of 3D electron density waves, under review, *Radio Sci*, 2007.

Lee, C. C., Shin-Yi Su, and B. W. Reinisch, An upward-moving thin layer in the equatorial F region observed by a digisonde, submitted, *Geophys. Res. Lett.*, 2007.

Paznukhov, V. V., B. W. Reinisch, P. Song, X. Huang, T. W. Bullett, and O. Veliz, Formation of an F3 layer in the equatorial ionosphere: A result from strong IMF changes, *J. Atmos. Solar-Terr. Phys.*, 69 (2007) 1292-1304.

Reinisch, B. W., P. Nsumei, X. Huang, and D. K. Bilitza, Modeling the F2 topside and plasmasphere for IRI using IMAGE/RPI and ISIS data, *Adv. Space Res.*, 39 (2007), 731-738.

Triskova, L., I. Galkin, V. Truhlik, and B.W. Reinisch, Application of seamless vertical profiles for use in the topside electron density modeling, *Adv. Space Res.*, 39, 774-778, 2007.

REFERENCES

- Bibl, K. and B. W. Reinisch, The universal digital ionosonde. *Radio Sci.*, 13, 519-530, 1978.
- Budden, K. G., "The propagation of radio waves", Cambridge University Press, 1988.
- Bullett, T.W., Mid-latitude ionospheric plasma drift: a comparison of digital ionosonde and incoherent scatter radar measurements at Millstone Hill, D. Eng. thesis, Dep. Of Eng., Univ. of Mass. Lowell, 1994.
- Buonsanto, M.J., Ionospheric Storms — A Review. *Space Science Reviews*, doi: 10.1023/A:1005107532631, 88,3-4, 1999.
- Buresova, D., Effects of geomagnetic storms on the bottomside ionospheric F region, *Adv. Space Res.*, 35, 429-439, 2005.
- Davies, K., *Ionospheric Radio*. Peter Peregrinus, London, 1990.
- Foster, J. C. and F. J. Rich, Prompt midlatitude electric field effects during severe geomagnetic storms, *J. Geophys. Res.*, 103, A11, 26367-26372, 1998.
- Fuller-Rowell, T. J., Codrescu, M. V., Moffett, R. J., and S. Quegan, Response of the thermosphere and ionosphere to geomagnetic storms, *J. Geophys. Res.*, 99, A3, 3893-3914, 1994.
- Haines, D.M., A portable ionosonde using coherent spread-spectrum waveforms for remote sensing of the ionosphere, D. Eng. thesis, Dep. Of Eng., Univ. of Mass. Lowell, 1994.
- Hocke, K. and K. Schlegel, A review of atmospheric gravity waves and travelling ionospheric disturbances: 1982-1995. *Ann. Geophys.*, 14, 9, 917-940, 1996.
- Huang, C.-S., Foster, J. C., and M. C. Kelley, Long-duration penetration of the interplanetary electric field to the low-latitude ionosphere during the main phase of magnetic storms, *J. Geophys. Res.*, A11309, doi:10.1029/2005JA011202, 2005
- Huang, X. and B. W. Reinisch, Vertical electron density profiles from the digisonde network, *Adv. Space Res.*, 18, 121-129, 1996.
- Jones, K. L. and H. Rishbeth, The origin of storm increases of mid-latitude F-layer electron concentration. *J. Atmos. Terr. Phys.*, 33, 391-401, 1971.
- McNamara, L. F., D. L. Cooke, C. E. Valladares, and B. W. Reinisch, Comparison of CHAMP and Digisonde plasma frequencies at Jicamarca, Peru, *Radio Sci.*, 42, RS2005, doi:10.1029/2006RS003491, 2007.

Mendillo, M., Storms in the ionosphere: Patterns and processes for total electron content. *Rev. of Geophys.*, 44, 4, 2006.

Prölss, G.W., On explaining the local time variation of ionospheric storm effects. *Ann. Geophys.*, 11, A1, 1-9, 1993.

Rawer, K. and K. Suchy, Radio Observations of the Ionosphere, *Handbuch der Physik*, 49/2, 1-546, 1967.

Rawer, K., Elektrische Wellen in einem geschichteten Medium, *Annalen der Physik*, 5, 386-416, 1939.

Reinisch, B. W., Modern Ionosondes, in *Modern Ionospheric Science*, Kohl, H., R. Rüster, and K. Schlegel (eds.), European Geophysical Society, 440-458, 1996.

Reinisch, B. W., D. M. Haines, K. Bibl, I. A. Galkin, X. Huang, D. F. Kitrosser, G. S. Sales, and J. L. Scali, Ionospheric sounding support of OTH radar, *Radio Sci.*, 32, 1681-1694, 1997.

Reinisch, B. W., J. L. Scali, and D. M. Haines, Ionospheric drift measurements with ionosondes, *Annali di Geofisica*, 41, 695-702, 1998.

Reinisch, B. W. and X. Huang, Deducing topside profiles and total electron content from bottomside ionograms, *Adv. Space Res.*, 27, 23-30, 2001.

Reinisch, B. W., P. Nsumei, X. Huang, and D. K. Bilitza, Modeling the F2 topside and plasmasphere for IRI using IMAGE/RPI, and ISIS data, *Adv. Space Res.*, 39, 731-738, 2007.

Richmond, A. D., M. Blanc, P. Amayenc, B. A. Emery, R. H. Wand, B. G. Fejer, R. F. Woodman, S. Ganguly, R. A. Behnke, and C. Calderon, An empirical model of quiet-day ionospheric electric fields at middle and low latitudes, *J. Geophys. Res.*, 85, 4658-4664, 1980.

Rishbeth, H., Kohl, H., and L. W. Barclay, A history of ionospheric physics and radio communications. In: Kohl, H.; Rüster, R., and Schlegel, K. (eds.) *Modern Ionospheric Science*. Katlenburg-Lindau: European Geophysical Society, 4-31, 1996.

Rishbeth, H., How the thermospheric circulation affects the ionospheric F2-layer. *J. Atmos. And Solar. Terr. Phys.*, 60, 14, 1385-1402. 1998.

Schunk, R. W., L. Scherliess, J.J. Sojka, and D. Thompson, Global Assimilation of Ionospheric Measurements (GAIM), *Radio Sci.*, 39, RS1S02, doi:10.1029/2002RS002794, 2004.

Zhou, Q. H., Two-day oscillation of the electron concentration in the lower ionosphere. *J. Atmos. Terr. Phys.*, V. 60, 1669-1677, 1998.